Thesis

Lia Hankla

Advisor: James Stone. Co-advisor: Frans Pretorius

May 1, 2017

Abstract

The diversity of plasmas in nature divides their study into many different regimes which are valid only within certain approximations. This paper attempts to extend the validity of one such regime (a fluids framework) to another (kinetic theory, for collisionless plasmas). The focus is more narrowly on astrophysical systems, where studies of collisionless plasmas very often use the fluid model which should theoretically not apply. Recent kinetic simulations of black hole accretion flows make radiatively inefficient accretion flows an ideal starting point to investigate the possibility of using a modified fluids closure to model collisionless plasmas. Study of these accretion flows is done through three-dimensional shearing box magnetohydrodynamic simulations with anisotropic viscosity and a maximum pressure anisotropy, a choice motivated by the aforementioned kinetic simulations. Results XXXXX and interesting because...(computation, conceptual, validate past work) ...

Contents

Chapter 1

Introduction

XX add pretty picture? XX protoplanetary disks? XX quote Broderick2011 that "ab initio calculations are beyond our present capability"

1.1 Overview

The discipline of plasma physics encompasses a vast variety of plasmas, stretching from earthly laboratory-made fusion plasmas to astrophysical plasmas such as the intracluster medium and accretion flows onto compact objects. What separates this discipline into different subfields is the immense variety of scales in terms of distance, density, and temperature. Although the theory of magnetohydrodynamics is scale-less, the different relationship between parameters means that the plasma inside a tokamak is not usefully described by the same set of equations as a disk of matter around the black hole at the center of the galaxy, where the distances are tens of orders of magnitude greater, densities are tens of orders of magnitude times smaller, and temperatures ten times lower (see Table 1.1).

All plasmas can in principle be described by a collection of equations describing the Lorentz force and other interactions on every single particle in the plasma. As can easily be imagined, however, the task of following billions of particles is intractable both analytically and computationally. Different sets of assumptions allow the impossible equations to be reduced to something useful in their respective situations. For instance, plasmas in which the particles do not collide often if at all (termed "weakly collisional" or "collisionless", respectively), need to be evolved using a distribution function that takes into account the spread of particle velocities: a kinetic theory.

In contrast, when the particles in a plasma collide many many times before they travel any meaningful distance in a system, the plasma can be treated as a fluid. Said fluid has only one, "bulk", velocity at any given point. The fluid mechanical approach is a further simplification of the full kinetic theory. As such, we would not expect a fluid treatment of collisionless plasmas to hold much weight.

It is perhaps surprising then, that it is common practice to do so. This unjustified assumption is not so hard to understand given the conceptual and practical simplification that the fluids model presents: instead of evolving six degrees of freedom, there are only three. It is also more intuitive to think about fluids as we have every day experience with them. So is this assumption valid? To date an investigation of the validity of this assumption seems to be absent from the astrophysical literature, although there might be such works among the fusion community.

The main goal of this thesis is to explore the viability of modelling a collisionless plasma with a modified fluid closure. If such an approximation is found to exist, then the assumptions of the past studies listed above are validated and the works stand on firmer theoretical ground. The approximation would also path the way for further studies of collisionless plasmas, easing not only the conceptual difficulty of a full kinetic theory but also the computational nuisance of particle-in-cell (PIC) simulations, which are limited by the extreme amount of resources they consume (a PIC simulation that takes millions of cpu-hours can be done in tens of cpu-hours using a fluid model).

1.2   Collisionless Plasmas

More formally, a collisionless plasma is one for which the particles on average travel longer than the scales one is interested in without colliding. This means that the length scales of interest (the radius of an accretion disk, for example, or the distance between the sun and the earth for the solar wind) L is much less than the mean free path λ_{mfp} of particles. In these cases the magnetic field is also strong enough such that the Larmor radius ρ is much less than both length scales of interest and the mean free path (a so-called "magnetized" plasma). We therefore have the ordering

$$\rho \ll \; L \lesssim \lambda_{mfp} \tag{1.1}$$

For weakly collisional plasmas, the mean free path is on the order of the length scales of interest. These orderings are opposed to fluid models in which both the mean free path and the Larmor radius are much less than the length scales of interest ($\lambda_{mfp} \ll L$, $\rho \ll L$).

Although the fluid description of a plasma (called "magnetohydrodynamics", MHD) has yielded a useful framework for fusion plasmas and the interstellar medium and connects nicely to the entire field of fluid dynamics (hydrodynamics—magnetohydrodynamics with no magnetic fields), the range of systems underneath the "collisionless plasma" umbrella is still quite large and therefore worth studying. Collisionless plasmas are most typically found in 1) the intracluster medium between galaxies, 2) radiatively inefficient accretion flows (RIAFs) around black holes, and 3) the solar wind [49]. Table 1.1 shows these collisionless plasma parameters in comparison to collisional plasmas such as magnetically-confined fusion plasmas. Here we often use the term "collisionless" also to describe weakly collisional systems such as RIAFs.

Collisionless plasma can be created and studied on earth in a laboratory by scaling parameters and using high-power lasers [15, 81, 18]. For instance, one experiment uses a density of 10^{18} cm^{-3} with a mean free path of 1 mm and a magnetic field of $7.4e4$ G to get the same ordering between parameters [15]. A brief overview of the three aforementioned types of weakly collisional/collisionless plasma follows.

The solar wind, a stream of particles released from the sun, is a weakly collisional plasma that has been regularly studied thanks to the Voyager missions and the Solar Wind Ion Analyzer aboard the MAVEN (Mars Atmosphere and Volatile Evolution Mission) [60]. Another solar wind experiment, Helios 2, observed anisotropic electron distribution and resulting anisotropic heat flux [73]. In analyzing the data, many papers acknowledge the inability of the MHD fluid model to capture kinetic effects. This assumption is often justified by likening the results of applying the model to hydrodynamic turbulence and noting success [55, 28] or claiming the inability to analyze kinetic instabilities theoretically [86, 76]. Others just accept the common standard and do not mention the fluid assumption [29].

The IntraCluster Medium (ICM), the gas that inhabits the space between galaxies in a galaxy cluster, is super hot and thus radiates in the X-ray regime. Again, papers do not justify the fluid assumption or simply do not

attempt to explain observations in the context of a broader model [21, 11, 57]. Recent investigations on the MagnetoThermal Instability (MTI) and Heat-flux-driven Buoyancy Instability (HBI) in the ICM have treated the ICM as a modified fluid [13, 67, 70, 69, 68].

Radiatively-inefficient accretion flows (RIAFs) have also often been treated as a fluid, usually with qualifications about such ad hoc assumptions [19, 34, 105, 39, 40, 102, 108, 84]. RIAFs are often found in a binary system, especially an x-ray binary system where a black hole is accreting matter off a white dwarf or other object. It is hoped that treating RIAFs correctly can explain observations of x-ray binary outbursts, or transitions from the dormant quiescent soft state to the active hard state and vice versa [78, 16, 17, 63, 82]. Another possible explanation is black hole jets [109, 22, 64], which are very complex phenomena (see [35] for a review), so we will stay away from x-ray binaries in this thesis.

Work involving accretion flows is also relevant to the supermassive black hole at the center of our galaxy, Sagittarius A*, as well as other, less well-resolved supermassive black holes like M87 [79, 65, 24, 9] and GX 339-4 [74]. The accretion disk around Sagittarius A* is many times dimmer than one might expect, knowing that the gravitational energy of in-falling matter must go somewhere—and where does it go, if not into radiation that can then be detected on Earth? Current models suggest that the accretion disk is heated up, resulting in a hot flow whose mean free path between particles is correspondingly large: a collisionless plasma. Such flows are termed "radiatively inefficient accretion flows" (RIAFs) and are thought to effectively model low-luminosity active galactic nuclei (LLAGN) such as Sagittarius A* [80, 8, 7, 19, 113].

This thesis will concentrate on collisionless plasmas in the context of RIAFs. This choice is motivated both by a recent paper that presents the first kinetic simulation of how accretion in a RIAF happens locally [52] and by hints at the inability of a fluid model to capture the correct growth rates of kinetic phenomena [90]. Although there has been some study on modified fluid closures to capture kinetic physics [93, 94, 89, 92], these studies use a different formalism. Now that a 3D kinetic simulation has been performed by Kunz et al. [52], a direct comparison between a modified fluid closure and kinetic theory is possible. The paper uses methods that are easily replicated using the Athena code developed by Stone et al. [101], in particular the same local shearing-box method [104]. A comparison is thus easily facilitated and

meaningful.

This paper is complementary to other current research in the field of accretion disk physics that often assumes a high degree of collisionality. For example, there is a push to include general relativity in accretion disk calculations in order to describe observations [58, 79, 96, 82, 63, 59]. This paper addresses the fundamental assumptions of these papers and assesses their validity, providing the groundwork for extending magnetohydrodynamics to relativistic systems and encompassing other effects important for reconciling observations and current models.

A fluid closure to kinetic physics has far-reaching consequences. If proper parameters are found that sufficiently imitate the kinetic physics of RIAFs, then this model can be extended to global simulations and enables the exploration of the parameter space of collisionless plasmas. Such exploration is currently prohibitively expensive computationally as mentioned previously because PIC simulations are required. If a fluid model is achieved, then the simulations are much more manageable, allowing for more thorough scans of, for example, magnetic field strength. A fluid model closure to kinetic physics is also interesting in a conceptual sense since it would mean that the six phase-space degrees of freedom could be reduced to only three position-space degrees of freedom.

The structure of this paper is as follows: the necessary background to understand the fundamental plasma physics question is explained in Chapter 2, which covers both important parameters such as the mean free path as well as the different models and closures that appear in various regimes, such as kinetic theory and magnetohydrodynamics. The next chapter zooms in to the astrophysical context of black hole accretion disks, motivating this paper's consideration of low luminosity active galactic nuclei through observational evidence and outlining basic accretion disk mechanics (Chapter 3). The actual physical mechanism for accretion, a linear MHD instability called the magnetorotational instability (MRI), is outlined in Chapter 4 using both analytic theory and the main tool of the rest of this thesis—simulations. By building from the simplest MHD theory (ideal MHD) to more complex, resistive MHD, principles of numerics such as choosing a proper box size and resolution are reviewed, allowing a smooth transition into the original research of this thesis found in Chapter 5. Chapter 5 uses the anisotropic viscosity along magnetic field lines as explained in Chapter 2.5 in the context explained in Chapter 3 in an attempt to capture kinetic physics in a

modified fluid closure.

	L (cm)	n (cm^{-3})	T (eV)	B (G)	ρ (cm)	λ_{mfp} (cm)	Description
ICM	6.2e23	5.0e-3	8.0e3	1.0e-6	1.3e10	9.5e21	KINETIC
RIAFs	1e13	1.0e2	2.0e3	1.0e-3	1e6	1e17	KINETIC
Solar wind	1.5e13	1.0e1	1.0e1	1.0e-4	4.6e6	1.2e13	KINETIC
ISM	3.1e20	1.0e0	1.0e0	5.0e-6	2.9e7	1.3e12	FLUID
JET	1.0e2	1.0e14	1.0e4	3.0e4	4.8e-1	1.4e6	FLUID

Table 1.1: Comparison of parameters of different plasmas found in space and on earth. ICM: intracluster medium. RIAF: radiatively-inefficient accretion flow. ISM: interstellar medium. JET: Joint European Torus (a tokamak). From [49, 100].

1.3 Codes: Athena4.2 and Pegasus

The systems under consideration in this thesis are extremely complicated and thus require the use of simulations to model on large time or length scales. Two codes are used for this purpose: one, an MHD solver, the other, a hybrid-kinetic particle-in-cell (PIC) code.

The code in use in Chapters 4 and 5 to simulate MHD systems is Athena4.2 (henceforth referred to as Athena). Athena, a response to the older code ZEUS, uses a higher-order Godunov scheme for flexibility and the constrained transport technique to ensure a divergence-free magnetic field. It is a highly-modularized grid-based code with additions such as adaptive mesh refinement (AMR) capabilities, special relativity, and dust [101, 103]. The shearing box approximation (as explained in Section 4.1.4) has also been implemented [104]. A new version of Athena, Athena++, more easily integrates general relativity and allows for better Riemannien solvers [110, 111].

For collisionless plasmas, the distribution function itself must be evolved. Such evolution is accomplished with a so-called "particle-in-cell" or PIC code. Because a fully-kinetic code usually requires compromising assumptions such as reduced speed of light or a smaller ion-to-electron mass ratio, hybrid-kinetic codes such as PEGASUS, the one used in [52] that this thesis compares its results to in Chapter 5, are perhaps more useful. PEGASUS itself treats electrons as a massless fluid, while ions are treated kinetically. This assumption is valid since ions are much hotter than electrons since

electrons can radiate efficiently [16]. PEGASUS is a second-order accurate code that uses a three-stage predictor-predictor-corrector algorithm for integration. It also uses the constrained transport method as Athena does to enforce a divergence-less magnetic field and implements the shearing box method [51].

Chapter 2

Plasma Physics: Context and Background

Understanding plasma physics is a topic worthy of a semester-long graduate class at least. This chapter briefly presents some basic plasma physics parameters and principles in Section 2.1, then examines the equations of motion and assumptions leading to the kinetic Vlasov equation and the so-called "hierarchy problem" in Section 2.2. The next sections look at different methods of dealing with the hierarchy problem (overview in Section 2.3), including more detailed examination of ideal MHD in Section 2.4 and Braginskii MHD in Section 2.5.

Remember, however, that the ultimate goal of this thesis is to study a particular phenomenon (the MagnetoRotational Instability, MRI) in a particular regime (anisotropic viscosity) of plasma physics. The link between the plasma physics discussed here and the astrophysics discussed in Chapter 3 comes in Chapters 4 and 5.

2.1   Properties of a Plasma

Plasma physics applies to a wide range of subject areas, from magnetic-confinement fusion pursuits like the tokamak ITER [38] and the stellarator Wendelstein 7-X [30] to a variety of astrophysical situations, including the sun's corona and protoplanetary disks. The uniting theme across these different disciplines is the plasma: so what exactly is a plasma?

A plasma is the so-called "fourth state of matter", coming after the gas

phase in the increasing kinetic energy hierarchy solid-liquid-gas: that is, the inetic energy of a plasma particle is much greater than its potential energy. A plasma is made up of neutrals and the result of the neutrals' ionization: that is, ions and electrons. The basic physics of single-particle motion in electric and magnetic fields (for example, ∇B drift and $E \times B$ drift) apply to every single particle. Given the enormous quantity of particles (as defined by the plasma parameter Λ in Section 2.1.1, working analytically or simulating such a situation for each individual particle is near impossible. Indeed, this is why the kinetic theory is so complicated and requires particle-in-cell simulations that use codes such as PEGASUS (Section 1.3). The task of Section 2.4 and Section 2.5 is to make simulations feasible via (modified) fluid equations.

2.1.1   Debye Length and Shielding

Since the ions and electrons in a plasma have opposite charge, they tend to attract, leading to the phenomenon of Debye shielding. Electrons of negative charge tend to cluster around a positive test charge and effectively shield the potential such that it is no longer Couloumbic ($V \propto 1/r^2$) but rather exponentially decays ($V \propto \frac{1}{r}e^{-r/\lambda_D}$). The distance over which the potential is screened is the total Debye length, which is related to the electron and ion Debye lengths λ_e and λ_i by:

$$\lambda_D^{-2} = \lambda_e^{-2} + \lambda_i^{-2} \tag{2.1}$$

where each species Debye length λ_j is given by

$$\lambda_j = \sqrt{\frac{T_j}{4\pi n_0 e^2}} \tag{2.2}$$

where T_j is the species equilibrium temperature in units of energy (Boltzmann's constant $k_b = 1$), n_0 is the density of each species far away from the test charge, and e is the charge on an electron. The exponential decay comes from the Boltzmann distribution since the system is at equilibrium. Detailed derivations can be found in any standard plasma physics introduction [62, 37?]. Magnetized plasmas are more important than, say, electric plasmas due to this shielding effect, since electric fields are shielded whereas magnetic fields will penetrate the plasma.

Going back to our definition of a plasma, requiring that the potential energy

of a particle is much less than its kinetic energy leads to the fact that the plasma parameter $\Lambda_s \equiv n_0 \lambda_s^3$ of each species is

$$\Lambda_s \gg 1 \tag{2.3}$$

This means that, in a plasma, there are many particles in a cube of the Debye length (alternative definitions define the plasma parameter as the number of particles within a sphere of radius the Debye length).

2.1.2 Mean Free Path and Collisions

Other important quantities include the mean free path λ_{mfp} of a plasma particle, that is, how far it travels on average before it collides with another particle. This is related to the thermal velocity $v_T = \sqrt{2T/m}$ and collision frequency ν by

$$\lambda_{mfp} = \frac{v_T}{\nu} = \frac{1}{\nu}\sqrt{\frac{2T}{m}} \tag{2.4}$$

Notice that since the mass of an electron is so small compared to that of an ion (made up of protons and neutrons), the electron thermal velocity is much greater than the ion thermal velocity.

The collision frequency ν can be found to depend on the temperature and density of a species as

$$\nu \sim nT^{-3/2} \tag{2.5}$$

Hence an increase in temperature leads to an increase in the mean free path of a particle because it decreases the collision frequency. In general, a higher collision rate simplifies calculations [37]. This is because collisions push particles towards the Maxwell-Boltzmann (or Maxwellian) distribution of thermal equilibrium. Ideal MHD assumes a Maxwellian distribution (see Section 2.4). It is departures from this equilibrium that complicate calculations: for example when the collisional frequency is different along magnetic field lines and across magnetic field lines, the result is Braginskii MHD (Section 2.5).

2.1.3 Magnetized Plasma Parameters

For a magnetized plasma, we can also define the gyrofrequency of a species Ω_s by looking at the equation of motion of a particle in a magnetic field, resulting in $\Omega_s = q_s B/m_s$ (Gaussian units). From the gyrofrequency we define the thermal gyroradius ρ_s as the radius of the circle of a particle traveling

at the thermal velocity: $\rho_s \equiv v_{T_s}/\Omega_s$. Note this is a factor of 2 different from the standard Larmor radius $\rho = v_\perp/\Omega_s$.

A magnetized plasma is one for which the dimensionless parameter $\delta \equiv \rho/L$ goes to zero. In this case, particles will follow orbits that oscillate many times about magnetic field lines as their guiding center travels along the field lines. In ideal MHD, both $\lambda_{mfp} \ll L$ and $\delta \ll L$ (Section 2.4), whereas Braginskii MHD takes $\rho \ll \lambda_{mfp} \ll L$ (Section 2.5) and a collisionless plasma has $\lambda_{mfp} \gtrsim L$.

As will be explained more later, the balance of magnetic pressure to gas pressure is also an important parameter. The plasma parameter, or β, as it is called, is given by:

$$\beta = \frac{8\pi P}{B^2} \tag{2.6}$$

where P is the plasma pressure and B is the magnetic field. β is generally much larger in astrophysical systems (order of hundreds or thousands) than in magnetic-confinement fusion, where β is usually around .01.

Having established some basic properties of a plasma, we can now investigate some theories to model them, starting with kinetic theory.

2.2   Vlasov Kinetic Theory

Kinetic theory generalizes the brute-force method of applying Maxwell's equations (and the Lorentz Force Law) to many particles. A derivation of the resulting equation is given in Appendix ??: for now we simply accept the result. The Vlasov equation is:

$$\frac{\partial f_s(\vec{x}, \vec{v}, t)}{\partial t} + \vec{v}_k \frac{\partial f_s}{\partial x_k} + \frac{q}{m}(\vec{E} + \frac{\vec{v}}{c} \times \vec{B})_k \frac{\partial f_s}{\partial v_k} = C[f_s] \tag{2.7}$$

where f_s is the phase-space density, or distribution function, and $\vec{v}$ is the velocity of a particle with charge q and mass m in electric and magnetic fields $\vec{E}$ and $\vec{B}$. The left side depends only smoothly-varying terms, whereas the right is spiky, being the average of products of delta functions. The right-hand side represents the interactions between individuals particles, and we can lump all these effects into the so-called "collision operator" $C[f]$. Entire graduate courses can be taught on the collision operator so we will not delve too much into it here.

Important properties of the collision operator can be found in introductory plasma physics texts such as Nicholson [62], Hazeltine and Waelbroeck [37], or Kunz [46]. Considering only collisions between two particles, the collision operator for a species s can be written as the sum of collisions between particles of two species s and s'. It then takes the form

$$C_s(f) = \sum_{s'} C_{ss'}(f_s, f_{s'}) \tag{2.8}$$

Returning to the distribution function, we define the distribution function to be normalized such that:

$$n_s(\vec{x}, t) = \int d^3 \vec{v} f_s(\vec{x}, \vec{v}, t) \tag{2.9}$$

Conservation laws emerge by taking different moments of the Vlasov equation and the collision operator. The k-th moment is defined as taking the integral $\int d^3 v \vec{v}^k f_s$.

Before we begin to take moments of the distribution function, however, it is useful to transform to the frame moving with the bulk velocity of the fluid. This relative velocity $\vec{w}$ is given by

$$\vec{w}_s \equiv \vec{v} - \vec{v}_s \tag{2.10}$$

where $\vec{v}$ is the bulk velocity of the fluid and $\vec{v}_s$ are the thermal motions of each species about this bulk velocity. Using transformations

$$\frac{\partial}{\partial t}\big|_{\vec{v}} = \frac{\partial}{\partial t}\big|_{\vec{w}} \cdot \frac{\partial}{\partial \vec{w}} = \frac{\partial}{\partial t}\big|_{\vec{w}} - \frac{\partial \vec{u}_s}{\partial t} \cdot \frac{\partial}{\partial \vec{w}}$$

$$\vec{\nabla}_x\big|_{\vec{v}} = \vec{\nabla}_x\big|_{\vec{w}} + (\nabla \vec{w})_{\vec{v}} \cdot \frac{\partial}{\partial \vec{w}} = \vec{\nabla}\big|_{\vec{w}} - (\nabla \vec{u}_s) \cdot \frac{\partial}{\partial \vec{w}}$$

Writing the derivative $\frac{D}{Dt_s} = \frac{\partial}{\partial t} + \vec{u}_s \cdot \vec{\nabla}$, the electric field in the moving frame $\vec{E}' = \vec{E} + \frac{1}{c}\vec{u}_s \times \vec{B}$, and $\vec{w}$-independent acceleration $\vec{a}_s = \frac{q_s}{m_s}\vec{E}' + \vec{g} - \frac{D\vec{u}_s}{Dt_s}$, we have the Vlasov equation:

$$\frac{Df_s}{Dt_s} + \vec{w} \cdot \vec{\nabla} f_s + \left[\vec{a}_s + \frac{q_s}{m_s c}\vec{w} \times \vec{B} - \vec{w} \cdot \vec{\nabla}\vec{v} \right] \cdot \frac{\partial f_s}{\partial \vec{w}} = C[f_s] \tag{2.11}$$

We can now take moments of Eq. 2.11 to attain conservation laws: for example, particle conservation arises from taking the zeroth-moment and

using Eq. 2.11 and the normalization equation 2.9:

$$\int d^3w \left[\frac{Df_s}{Dt} + \vec{w} \cdot \vec{\nabla} f_s + a_i \frac{\partial}{\partial w_i} f_s + \frac{q_s(\vec{w} \times \vec{B})_i}{m_s c} \frac{\partial f_s}{\partial w_i} - (\vec{w} \cdot \vec{\nabla}\vec{v})_i \frac{\partial f_s}{\partial w_i} \right]$$

$$= \int d^3w \; C_s = 0$$

$$= \frac{Dn_s}{Dt} + \frac{\partial}{\partial x_i} \int d^3w \; w_i f_s$$

$$+ \int d^3w \; a_{si} \frac{\partial f_s}{\partial w_i} + \int d^3w \; \frac{q_s}{m_s c}(\vec{w} \times \vec{B})_i \frac{\partial f_s}{\partial w_i}$$

$$- \int d^3w \; (\vec{w} \cdot \nabla\vec{v})_i \frac{\partial f_s}{\partial w_i} = 0$$

The second term

$$\frac{\partial}{\partial x_i} \int d^3w \; w_i f_s = 0$$

by definition of $\vec{w}$. The third and fourth terms are zero from integration by parts:

$$\int d^3w \; a_{si} \frac{\partial f_s}{\partial w_i} + \int d^3w \frac{q_s}{m_s c}(\vec{w} \times \vec{B})_i \frac{\partial f_s}{\partial w_i} = 0$$

This leaves us with

$$\frac{Dn_s}{Dt} = \int d^3w \; (\vec{w} \cdot \nabla\vec{v})_i \frac{\partial f_s}{\partial w_i} = -n_s \nabla \cdot \vec{v}$$

also by using integration of parts [46]. This leaves us with our continuity equation:

$$\frac{\partial n_s}{\partial t} + \nabla \cdot (n_s \vec{v}) = 0 \tag{2.12}$$

This equation is for each individual species.

Similarly, taking the first-moment of Eq. 2.11 yields conservation of momentum for each species:

$$m_s \frac{\partial n_s \vec{v}_s}{\partial t} + \nabla \cdot \vec{P}_s - e_s n_s (\vec{E} + \vec{v}_s \times \vec{V}) = \vec{F}_s \tag{2.13}$$

Here, $\vec{F}_s$ is the friction force, that is, the force experienced due to collisions. It is the sum over all colliding species s': $\vec{F}_s = \sum_{s'} \vec{F}_{ss'}$. In equation form the force due to a species s' is simply the first moment of the collision function:

$$\vec{F}_{ss'} = \int d^3v m_s \vec{v} C_{ss'} \tag{2.14}$$

16

In Eq. 2.13, $\vec{P}_s$ is the second-order moment of the distribution function, the pressure (or stress, when not in the bulk fluid frame) tensor:

$$\vec{P}_s(\vec{x}, t) = \int d^3v f_s(\vec{x}, \vec{v}, t) m_s \vec{v}\vec{v} \tag{2.15}$$

Summing Eq. 2.13 over species gives the full conservation of momentum equation, for which the right-hand side of Eq. 2.13 is zero.

The second-moment of the Vlasov equation (contracted) gives a species energy conservation equation:

$$\frac{\partial}{\partial t}\left(\frac{3}{2}p_s + \frac{1}{2}m_s n_s v_s^2\right) + \nabla \cdot \vec{Q}_s - e_s n_s \vec{E} \cdot \vec{v}_s = W_s + \vec{v}_s \cdot \vec{F}_s \tag{2.16}$$

Here, $W_s = \sum_{s'} W_{ss'}$ is the total kinetic energy change of species s due to collisions with all other species. $W_{ss'}$ is the change in kinetic energy experienced by species s due to collisions with species s':

$$W_{ss'} = \int d^3v \frac{1}{2} m_s v_s^2 C_{ss'} \tag{2.17}$$

The p_s of Eq. 2.16 is given by the trace of the pressure tensor in the reference frame of bulk motion of the fluid. Then we have

$$\vec{p}_s(\vec{x}, t) = \int d^3v f_s(\vec{x}, \vec{v}, t) m_s \vec{w}_s \vec{w}_s \tag{2.18}$$

$$p_s = \frac{1}{3} Tr(\vec{p}_s) \tag{2.19}$$

The $\vec{Q}$ in Eq. 2.16 is the heat flux tensor in the bulk fluid frame, or energy flux density in the lab frame. It is the third moment of the distribution function [37]:

$$\vec{Q}_s(\vec{x}, t) = \int d^3v f_s(\vec{x}, \vec{v}, t) \frac{1}{2} m_s v^2 \vec{v} \tag{2.20}$$

At this point a pattern has been established: every conservation law involves a higher moment of the distribution function. The evolution of density (Eq. 2.12) involves velocity, evolution of velocity (Eq. 2.13) involves the pressure tensor $\vec{P}$, evolution of the pressure (Eq. 2.16) involves the heat flux tensor $\vec{Q}$, and so on. This pattern of always involving higher moments of the distribution function does not simply disappear. Rather, it is a central problem of plasma physics known as the BBGKY hierarchy. It is various choices to "close" this loop of higher moments that defines different theories,

including the standard ideal or "single-fluid" MHD.

The next section describes the various paths one can take to close the moment equations 2.12, 2.13, and 2.16. This path will lead to both ideal MHD (Section 2.4) and Braginskii MHD (Section 2.5).

2.3 Overview of Moment Equation Closures

As just mentioned, the moment equations as they stand are somewhat useless because they generate an infinite set of equations. We therefore now consider methods to actually use these equations. These methods fall broadly into three categories: truncation, cases with special values for the distribution function or stress tensor, and asymptotic methods.

The most straightforward (and least-often employed, for obvious reasons) solution is to simply truncate the hierarchy. For example, just call the heat flux tensor $\vec{Q} = 0$. This method can lead to useful intuition, but also means that the amount of error is not well-accounted for at all [37].

Special cases allow the moment equations to close. For example, a Maxwellian distribution function depends only on $n_s(\vec{x}, t)$, $T_s(\vec{x}, t)$, and $v_s(\vec{x}, t)$ so only the first three moment equations are needed. The distribution is Maxwellian when the system is in local thermal equilibrium [37]. Although this condition is somewhat difficult to characterize, generally a higher degree of collisionality means that the Maxwellian is a better approximation. As mentioned previously, collisions tend to mix up particle velocity and therefore push the system towards equilibrium. This Maxwellian approximation can be used to give a first-order approximation even in collisionless systems, as will be examined in Section 2.5.

A second special case is that of a cold plasma, for which the pressure tensor is zero. This is equivalent to a plasma without thermal motions, and so dynamics depend only on the density and velocity of each species. This closure is generally useful for considering what kinds of waves can occur [37].

The last closure method is that of asymptotics. This method generally assumes an ordering of certain parameters and expands about small values; which parameters are large or small depends on the exact type of asymptotic closure. This is the method discussed in Sections 2.4 and 2.5 below.

The standard so-called "MHD ordering" assumes a magnetized plasma and takes $\delta \equiv \rho/L \ll 1$. The motion perpendicular to field lines does not disappear; since there is still $E \times B$ drift, we assume the drift speed is on the order of the thermal speed, leading to the assumption that

$$\frac{E_\perp}{B} \sim v_t \tag{2.21}$$

Taking this drift to zero is called the drift ordering and will not be discussed here. A good treatment is given in [37].

Assumptions from this point forward divide MHD into its different branches (for example, single-fluid ideal MHD and Braginskii MHD) and will be discussed in subsequent sections.

2.4   Single-fluid MHD

In single-fluid MHD, all species are treated as a single fluid. That is, to lowest-order they all have the same temperature and flow velocity and we average out the individual particles' positions and velocities. The important quantities are bulk variables, like the mean flow of the fluid, density, and pressure (one can already see how this variables might not make as much sense for an extremely diffuse plasma such as the weakly collisional ones described in Chapter 1).

To begin with, we assume quasi-neutrality:

$$\sum_s n_s q_s = 0 \tag{2.22}$$

This is usually a good simplification since plasmas are usually overall neutral in nature. This assumption makes the Maxwell equation for the divergence of $\vec{E}$ irrelevant, since the enclosed charge is zero and stays zero automatically.

As mentioned earlier, the characteristic velocity of particles in our system is the thermal velocity. This is generally much slower than the speed of light, and so in Ampere's law we can neglect the displacement current and use:

$$\nabla \times \vec{B} = \mu_0 \vec{J} \tag{2.23}$$

Note that it is possible to include general relativity in these calculations [**? ?**]; however, as mentioned in the introduction, this thesis is concerned with

the limit in which general relativity is excessive.

In the MHD ordering mentioned above, the velocity perpendicular to field lines is comparable to the thermal velocity and hence dominates whatever other perpendicular velocities due to collisions or other effects there may be. The fluid velocity is thus given by $\vec{v} = \vec{v}_{\parallel} + \vec{v}_E$ where $\vec{v}_E$ is the $E \times B$ drift velocity. This condition is captured in the MHD version of Ohm's law:

$$\vec{E} + \vec{v} \times \vec{B} \tag{2.24}$$

The last of Maxwell's equations is also needed. Combined with the moment equations from Section 2.2, we have the complete set of equations:

$$\frac{D\rho}{Dt} + \rho \nabla \cdot \vec{v} = 0 \tag{2.25}$$

$$\frac{Dp}{Dt} + \frac{5}{3} p \nabla \cdot \vec{v} = 0 \tag{2.26}$$

$$\rho \frac{D\vec{v}}{Dt} + \nabla p - \vec{J} \times \vec{B} = 0 \tag{2.27}$$

$$\vec{E} + \vec{V} \times \vec{B} = 0 \tag{2.28}$$

$$\nabla \times \vec{B} = \mu_0 \vec{J} \tag{2.29}$$

$$\nabla \times \vec{E} + \frac{\partial \vec{B}}{\partial t} = 0 \tag{2.30}$$

For obvious reasons, Eq. 2.25 is known as the continuity equation, Eq. 2.26 as the internal energy equation (for a gas with adiabatic index/ratio of specific heats $\gamma = 5/3$), and Eq. 2.27 as the momentum equation.

A bit of notation: here, the "convective derivative" $\frac{D}{Dt} = \frac{\partial}{\partial t} + \vec{v} \cdot \nabla$, where $\vec{v}$ is the center of mass motion of the fluid. This derivative accounts for both temporal and spatial variation as a fluid element moves along with the bulk motion of the rest of the fluid.

Notice that Eq. 2.28 and Eq. 2.29 can be used in Eqs. 2.25, 2.26, and 2.27 to achieve a more compact form. Using Eq. **??**:

$$\nabla \times \vec{E} = -\nabla \times (\vec{v} \times \vec{B})$$
$$= -(\vec{B} \cdot \nabla \vec{v} - \vec{v} \cdot \nabla \vec{B} - B \nabla \cdot \vec{v})$$

and so Faraday's law Eq. 2.30 becomes

$$\frac{D\vec{B}}{Dt} - \vec{B} \cdot \nabla \vec{v} + \vec{B} \nabla \cdot \vec{v} = 0 \tag{2.31}$$

which is known as the induction equation. Similarly, the momentum equation can be modified using

$$\mu_0 \vec{J} \times \vec{B} = \vec{B} \cdot \nabla \vec{B} - \frac{1}{2} \nabla B^2 \tag{2.32}$$

The new momentum equation is thus:

$$\rho \frac{D\vec{v}}{Dt} + \nabla \left(p + \frac{B^2}{2\mu_0} \right) - \frac{1}{\mu_0} \vec{B} \cdot \nabla \vec{B} = 0 \tag{2.33}$$

We can see that a combination of the continuity and internal energy equation yields the adiabatic law for an ideal gas by eliminating $\nabla \cdot \vec{v}$:

$$
\begin{aligned}
0 &= \frac{Dp}{Dt} + \frac{5}{3} p \nabla \cdot \vec{v} = \frac{Dp}{Dt} - \gamma \frac{p}{\rho} \frac{D\rho}{Dt} \\
0 &= \frac{1}{p} - \frac{\gamma}{\rho} \frac{D\rho}{Dt} = \frac{D}{Dt} \ln p - \gamma \frac{D}{Dt} \ln \rho \\
&= \frac{D}{Dt} \ln \left(\frac{P}{\rho^\gamma} \right) \\
0 &= \frac{D}{Dt} \left(p \rho^{-5/3} \right)
\end{aligned}
\tag{2.34}
$$

where $\gamma = 5/3$ was taken in the first line. The evolution used in Chapter 4 uses such an adiabatic equation of state.

Since the plasma is perfectly conducting, the magnetic field lines cannot diffuse (this will be changed below in Section 2.4.1). This means that the field lines are effectively frozen into the plasma: the phenomenon is appropriately called "flux-freezing", or alternatively as Alfven's Theorem (proof in Appendix **??**). Flux-freezing has important consequences for turbulence, since if a fluid particle is perturbed slightly, it will drag the magnetic field line with it (see Chapter 4.1).

We have now collected all of the equations of MHD. We can summarize the assumptions as follows:

- The MHD ordering: the $E \times B$ drift velocity is on the order of the thermal velocity. This leads to the MHD Ohm's Law (Eq. 2.28)

- Non-relativistic. This leads to the neglect of the displacement current in Ampere's law (Eq. 2.29).

- Quasi-neutrality (Eq. 2.22). This incorporates Gauss's law into an assumption.

- Magnetic plasma: $\delta \to 0$. This means that we can separate particle orbits into guiding center and gyro-motion about the field lines.

- Isotropic pressure: the heat flux tensor disappears.

- *Ideal* MHD: resistance is zero.

It is worth noting that, like hydrodynamics, magnetohydrodynamics has no characteristic length scale. This is what gives hydrodynamics the power to describe objects on the scales of hurricanes just as accurately as those on the scales of the water flushing down a toilet. In MHD, it means that simulations are not as affected by the choice of units, unlike in non-ideal MHD where there is a characteristic length scale. Removing this last assumption is the topic of Section 2.4.1.

2.4.1 Non-ideal MHD

Non-ideal MHD modifies the ideal MHD equations by simply adding resistivity to the MHD Ohm's law and viscosity to the induction equation. That is, Eq. 2.28 becomes

$$\vec{E} + \vec{v} \times \vec{B} = \eta \vec{J} \tag{2.35}$$

where η is the resistivity of the plasma. Basically, it provides a dissipative term, as can be seen by putting this into Faraday's law 2.31:

$$\frac{D\vec{B}}{Dt} - \vec{B} \cdot \nabla \vec{v} + \vec{B} \nabla \cdot \vec{v} = \frac{\eta}{\mu_0} \nabla^2 \vec{B} \tag{2.36}$$

The last term takes the form of a diffusion operator. There is no longer such stringent flux-freezing; rather, the magnetic field lines slip with respect to the rest of the plasma. Forms of this phenomena, for example the Hall effect or ambipolar diffusion, help explain how stars forming from magnetized clouds end up with so little magnetic flux themselves [43].

Notice that now the equations do have a characteristic length scale, unlike in ideal MHD. The magnetic field diffuses out on the time scale of

$$\tau_R = \frac{\mu_0 L^2}{\eta} \tag{2.37}$$

This time scale will become important in Chapter 4: for instance, if the dissipation time scale is shorter than characteristic time scales of the system (such as orbital time), then the magnetic field will decrease in energy, hindering the development of a magnetic dynamo.

Just as resistivity smooths out the magnetic field, viscosity smooths out the velocity field by eliminating smaller eddy currents. It takes the same Laplacian form in the momentum equation, which becomes:

$$\rho \frac{D\vec{v}}{Dt} + \nabla \left(p + \frac{B^2}{2\mu_0} \right) - \frac{1}{\mu_0} \vec{B} \cdot \nabla \vec{B} + \nu \nabla^2 \vec{v} = 0 \qquad (2.38)$$

where ν is the viscosity parameter. The more rigorous form enters as the divergence of the viscous stress tensor T_{ik}:

$$T_{ik} = \rho \nu \left(\frac{\partial v_i}{\partial x_k} + \frac{\partial v_k}{\partial x_i} - \frac{2}{3} \delta_{ik} \nabla \cdot \vec{v} \right) \qquad (2.39)$$

as in [26]. However, since we are concerned only with isotropic viscous forces, the form reduces to that of Eq. 2.38.

The importance of resistivity and viscosity has been explored in a number of papers [26, 53, 27] and plays an important role in the physics accretion, as will be discussed in Chapter 3. Resistivity in the MHD equations leads to various effects like ambipolar diffusion, the hall effect, and normal Ohmic dissipation. For an overview see Kunz [47].

2.4.2 Dimensionless Numbers in Non-ideal MHD

With the introduction of length scales comes the introduction of certain dimensionless numbers that characterize a fluid or plasma flow. For example, in hydrodynamics the Reynolds number is given by the ratio of inertial forces to viscous forces and can be written as

$$\mathrm{Re} = \frac{c_0 L}{\nu} \qquad (2.40)$$

where c_0 is the sound speed or other characteristic velocity in the fluid and ν is the viscosity. Like above, L is a characteristic length scale. In Chapter 4, this will be taken as the scale height of the disk (defined in Section 3.3.3). This results in the interpretation of the Reynolds number as the amount of dissipation on disk length scales in one sound crossing: if c_0/H is (on the

order of) the time it takes for a sound wave to cross the disk and dissipation $\eta\nabla^2$ is given roughly as H^2/η, we have

$$\text{Re} = \frac{c_0}{H}\frac{H^2}{\eta} \tag{2.41}$$

In magnetohydrodynamics, we can define the magnetic Reynolds number as how important induction and advection of the magnetic field is compared to momentum advection of a fluid: the advection of B is given as a characteristic velocity v crossed with the magnetic field $(\vec{v}\times\vec{B})$ and resistive diffusion scales are on the order of $\eta\vec{J}\sim\eta\nabla\times\vec{B}\sim\eta B/L$ and so we have:

$$\text{Re}_\text{M} = \frac{\vec{v}\times\vec{B}}{\eta B/L} = \frac{vL}{\eta} \tag{2.42}$$

The ratio of the magnetic Reynolds number to the Reynolds number is called the magnetic Prandtl number:

$$\text{Pm} = \frac{\text{Re}_\text{M}}{\text{Re}} = \frac{\nu}{\eta} \tag{2.43}$$

The magnetic Prandtl number accordingly measures how important viscous diffusion is relative to resistive diffusion. Higher Prandtl number means viscous dissipation is more important, and thus the velocity field is smoothed more than the magnetic field. In such situations we can expect more small-scale magnetic field eddies than velocity eddies. The hydrodynamic Prandtl number measures the importance of viscosity as compared to thermal diffusion and heat conduction rather than resistivity [?].

These dimensionless numbers are important in determining properties of accretion flows in Chapter 4: for example, low magnetic Prandtl number will result in a decay of magnetic energy over time.

2.5   Braginskii MHD

This section explores a description of strongly magnetized, weakly collisional plasmas. The appropriate closure to the moment equations is provided by assuming conservation of certain adiabatic invariants like the magnetic moment, described in Section 2.5.2.

The Braginskii closure uses the assumptions that the time between collisions, while not zero, is much larger than typical time scales. Equivalently,

the collisional frequency is much greater than other characteristic frequencies of the system. The appropriate limits are:

$$\rho \ll \lambda_{mfp} \ll L \tag{2.44}$$

Note that weakly collisional systems have mean free paths comparable to or larger than the length scales of the system: we therefore have no apparent reason to trust Braginskii MHD in a weakly collisional regime! Such is the motivation of this thesis: we shall investigate whether we can actually accomplish a meaningful approximation.

Because the magnetic field is so strong and the gyromagnetic radius is so small compared to the mean free path, we can write the motion of particles as a sum of the guiding center motion and the gyrotropic motions about the field lines. Section 2.5.1 will rigorously show how we can trace out the gyromotion of the particle to yield a pressure tensor purely in terms of the frame along and perpendicular to magnetic field lines. An explanation of why pressure anisotropy can arise is offered by the adiabatic invariants, explained in Section 2.5.2. Writing everything in terms of this pressure anisotropy, we then explore two different closures and their impact on the MHD equations: the first, double adiabatic or Chew-Goldberger-Low for collisionless plasmas [14] in Section 2.5.3, and the second, the Braginskii closure for weakly collisional plasmas in Section 2.5.4. After exploring the consequences of said pressure anisotropy in the MHD equations, we introduce the modified closure that attempts to capture certain kinetic physics (Section 2.5.5). XX

2.5.1 Anisotropic Pressure Tensor

A pressure anisotropy is a source of free energy that will push the distribution function back to a Maxwellian; how then, does the anisotropy arise in the first place? A more detailed derivation is given in Appendix [?], but it is intuitive enough to define

$$p_{\parallel} \equiv m \int d^3 w \ w_{\parallel}^2 f(w_{\parallel}, w_{\perp}) \tag{2.45}$$

$$p_{\perp} \equiv m \int d^3 w \ \frac{w_{\perp}^2}{2} f(w_{\parallel}, w_{\perp}) \tag{2.46}$$

and the pressure tensor as

$$\begin{pmatrix} p_{\parallel} & 0 & 0 \\ 0 & p_{\perp} & 0 \\ 0 & 0 & p_{\perp} \end{pmatrix} \tag{2.47}$$

if $\hat{x} = \hat{b}$ is along the magnetic field and $w_\parallel$ and $w_\perp$ are the velocity along and across the magnetic field lines, respectively. Note that the isotropic pressure $p = \frac{2}{3}p_\perp + \frac{1}{3}p_\parallel$ and hence $p_\perp = p + \frac{1}{3}(p_\perp - p_\parallel)$ and $p_\parallel = p - \frac{2}{3}(p_\perp - p_\parallel)$.

Rigorously what follows is an expansion of the distribution function about a Maxwellian (see, e.g., [61]). However, we take a more intuitive approach here and simply argue for adding collisional terms to the evolution equations for the pressures, as illustrated below.

2.5.2 Adiabatic Invariants

Although we have made progress in showing that the pressure tensor is anisotropic, the problem of closure remains. However, we can now focus on finding an expression for the pressure anisotropy $p_\perp - p_\parallel$ rather than the pressure p. In ideal MHD, we had closed the loop by assuming isotropic pressure p. Using the continuity equation and remembering $\gamma = 5/3$, this resulted in the entropy equation 2.34

$$0 = \frac{D}{Dt} \ln \left(\frac{P}{\rho^\gamma} \right)$$

Now, however, we must find a relationship between the pressure perpendicular and parallel to the magnetic field lines. We achieve this by considering adiabatic invariants.

Adiabatic Invariants are quantities that are "conserved" in the sense that they stay the same when changes in a system happen slowly enough. Two such quantities will be important in establishing the so-called "double-adiabatic" closure, which assumes pressure isotropy, and then its modification, leading to the Braginskii closure. Here we simply state the invariants; their conservation is derived in any number of plasma physics texts [62].

It turns out that the magnetic moment μ is conserved, where

$$\mu = \frac{1}{2} m \frac{w_\perp^2}{B}$$

For this reason μ is also known as the first adiabatic invariant. The next quantity has to do with magnetic mirrors and is called either the second adiabatic invariant or the mirror constant. It is given by

$$J \equiv m \oint w_\parallel dl$$

26

We claimed that adiabatic invariants were "invariant" as long as the system changed slowly enough: now we can quantify this statement.

Since the magnetic moment is based on the strength of the magnetic field in relation to the Larmor frequency Ω, we need the spatial and temporal changes of the magnetic field to be slow relative to Ω. In equation form, we require:

$$\left|\frac{D \ln B}{Dt}\right| \ll \Omega$$

The mirror constant depends on how fast particles bounce back and forth in the mirror, or the bounce frequency ω_b. We thus need the magnetic field to change spatially and temporally on time scales much slower than the bounce frequency:

$$\left|\frac{D \ln B}{Dt}\right| \ll \omega_b$$

Following Kunz [45], we can now estimate the average values of these adiabatic invariants. The magnetic moment average value is defined as

$$\langle \mu \rangle = \frac{\int d^3 w \ f\mu}{\int d^3 w \ f} = \frac{\frac{1}{B} \int d^3 w \ \frac{1}{2} m w_\perp^2 f}{\int d^3 w \ f}$$

Remembering that the perpendicular pressure is defined as the top integral and the bottom integral is defined to be the number density, we have

$$\langle \mu \rangle = \frac{p_\perp}{Bn} = \frac{T_\perp}{B} \tag{2.48}$$

after noting that $T_\perp = p_\perp/n$. Similarly, for the mirror constant we can define a length of the magnetic mirror to be B/n since the flux is constant. The mirror constant average value then becomes

$$\langle J^2 \rangle = \frac{\int d^3 w \ f J^2}{\int d^3 w \ f} = \frac{m^2 B^2}{n^2} \frac{\int d^3 w \ f w_\parallel^2}{\int d^3 w \ f}$$

$$= \frac{mB^2}{n^3} p_\parallel = \frac{B^2}{n^2} T_\parallel m \tag{2.49}$$

with $T_\parallel = p_\parallel/n$. We have found now that a change in the magnetic field strength changes the pressure perpendicular to the magnetic field lines, while a change in the square of the magnetic field density B^2/n^2 results in a change of the pressure parallel to the magnetic field lines. The first equivalence is a rather good assumption, whereas the second is often violated, as evidenced by the rather sketchy approximation of the mirror length. However, we can still use these adiabatic invariants to close the moment equations.

2.5.3 Double Adiabatic Closure

Using the adiabatic invariant average value equations above, we can come up with an equation for the evolution of the pressure anisotropy, again following Kunz [45]. We note that Eqns. 2.48 and 2.49 yield evolution equations

$$\frac{D}{Dt}\left(\frac{T_\perp}{B}\right) = \frac{D}{Dt}\left(\frac{p_\perp}{nB}\right) = 0$$

$$\frac{D\ln p_\perp}{Dt} = \frac{D\ln n}{Dt} + \frac{D\ln B}{Dt} \qquad (2.50)$$

for the magnetic moment and

$$\frac{D}{Dt}\left(\frac{T_\parallel B^2}{n^2}\right) = \frac{D}{Dt}\left(\frac{p_\parallel B^2}{n^3}\right) = 0$$

$$\frac{D\ln p_\parallel}{Dt} = 3\frac{D\ln n}{Dt} - 2\frac{D\ln B}{Dt} \qquad (2.51)$$

for the mirror constant. The pressure anisotropy is then given by

$$\frac{D\ln p_\perp}{Dt} - \frac{D\ln p_\parallel}{Dt} = 3\left(\frac{D}{Dt}\ln\frac{B}{n^{2/3}}\right)$$

The right hand side, the adiabatic invariance, produces the pressure anisotropy in the left hand side. We therefore conclude that, without collisions, anisotropy is produced uncontrollably. Alternative evolution equations are given in Strumik et al. [106].

This double-adiabatic or Chew-Goldberger-Low (CGL) closure was originally developed for fusion devices. Unfortunately, there are several problems with this result when applied to astrophysics, partly because the magnetic fields are more tangled and the magnetic fields are more tangled [93]. First, it does not constrain collisions at all along magnetic field lines [14]. Many have argued that this means the closure is not physical, since in principle heat flow along magnetic field lines can be arbitrarily large [54, 37, 107]. As a result, the closure does not give the correct thresholds for kinetic instabilities like the mirror threshold (important later on), or the necessary stabilization at small scales [71], which is particularly important for the present thesis.

2.5.4 Braginskii MHD Equations

XX standardize notation (n vs. rho), explain entropy to internal energy

The above result for the pressure anisotropy closure was for a collisionless plasma. In the Braginskii closure, we now introduce collisions. Following Kunz [45] however, we assume that the plasma is only weakly collsional and so in combination with Eq. 2.44 we have

$$\Omega \gg \nu_{coll} \gg \frac{1}{t_{dyn}}$$

where ν_{coll} is the collision frequency and t_{dyn} is a dynamical time scale of the system. We know that collisions push the distribution function back to a Maxwellian; therefore, we keep the pressure anisotropy small and modify Eqs. 2.50 and 2.51 to account for this small difference, moderated by the small parameter ν_{coll}:

$$\frac{Dp_\perp}{Dt} = p_\perp \left(\frac{D \ln Bn}{Dt} \right) - \nu_{coll}(p_\perp - p)$$

$$\frac{Dp_\parallel}{Dt} = p_\parallel \left(\frac{D \ln B^{-2}n^3}{Dt} \right) - \nu_{coll}(p_\parallel - p)$$

These equations lead to a pressure anisotropy evolution:

$$\frac{D}{Dt}(p_\perp - p_\parallel) = p_\perp \frac{D \ln Bn}{Dt} - p_\parallel \frac{D \ln B^{-2}n^3}{Dt} - \nu_{coll}(p_\perp - p_\parallel)$$

$$= p \frac{D}{Dt} \ln \frac{B^3}{n^{2/3}} - \nu_{coll}(p_\perp - p_\parallel)$$

With the Braginskii ordering, the derivative of the pressure anisotropy is effectively zero $\left(\frac{D(p_\perp - p_\parallel)}{Dt} \sim (p_\perp - p_\parallel)\frac{1}{t_{dyn}} \ll \nu_{coll} \right)$, leaving the final Braginskii closure for the pressure tensor:

$$p_\perp - p_\parallel = \frac{3p}{\nu_{coll}} \frac{D}{Dt} \ln \frac{B}{n^{2/3}} \qquad (2.52)$$

This closure shows how the pressure anisotropy produced by adiabatic invariance as in the double adiabatic closure is decreased by collisions.

We can now write the MHD equations in terms of this closure. The in-

ternal energy or entropy equation is straightforward:

$$\frac{Dp}{Dt} = \frac{2}{3}\frac{Dp_\perp}{Dt} + \frac{1}{3}\frac{Dp_\parallel}{Dt}$$

$$- \nu_{coll}\left(\frac{2}{3}p_\perp + \frac{1}{3}p_\parallel - p\right)$$

$$= \frac{5p}{3}\frac{D\ln n}{Dt} + \frac{2}{3}(p_\perp - p_\parallel)\frac{D\ln B^{-2}n^3}{Dt}$$

$$\frac{D}{Dt}\ln\frac{P}{n^{5/3}} = \frac{2}{3}\left(\frac{p_\perp - p_\parallel}{p}\right)\frac{D}{Dt}\ln\frac{B}{n^{2/3}}$$

$$\frac{p}{\gamma-1}\frac{D}{Dt}\ln\frac{P}{n^\gamma} = (p_\perp - p_\parallel)\frac{D}{Dt}\ln\frac{B}{n^{\gamma-1}}$$

where the last line takes $\gamma = 5/3$. The Braginskii closure uses Eq. 2.52 to make the right-hand side of the last equation into $(p_\perp - p_\parallel)^2\nu_{coll}/3p$. Note that this reduces to the adiabatic gas law when $\nu_{coll} \to 0$.

All this effort is more elucidating if we massage these equations into a better form: in particular, using the continuity equation and induction equation (where : contracts over an index) we have

$$\frac{D\ln n}{Dt} = -\nabla \cdot \vec{u}$$

$$\frac{D\ln B}{Dt} = \hat{b}\hat{b} : \nabla\vec{u} - \nabla \cdot \vec{u}$$

$$= (\hat{b}\hat{b} - \vec{\mathbb{I}}) : \nabla\vec{u}$$

gives the Braginskii closure as

$$p_\perp - p_\parallel = \frac{3p}{\nu_{coll}}\frac{D}{Dt}\ln\frac{B}{n^{2/3}}$$

$$= \frac{3p}{\nu_{coll}}\left[(\hat{b}\hat{b} - \vec{\mathbb{I}}) - \frac{2}{3}(-\vec{\mathbb{I}})\right] : \nabla\vec{u}$$

$$= \frac{3p}{\nu_{coll}}\left(\hat{b}\hat{b} - \frac{\vec{\mathbb{I}}}{3}\right) : \nabla\vec{u} \qquad (2.53)$$

Plugging this closure into the entropy equation yields

$$\frac{3}{2}p\frac{D\ln pn^{-5/3}}{Dt} = \frac{3p}{\nu_{coll}}\left[\left(\hat{b}\hat{b} - \frac{\vec{\mathbb{I}}}{3}\right) : \nabla\vec{u}\right]^2$$

The right hand side of the entropy equation in the form of $|\nabla \vec{u}|^2$ represents viscous heating. Clearly, the viscous heating is anisotropic. But what does this mean? Examining the right hand side more closely, we see that the vector $\hat{b}\hat{b} - \vec{\mathbb{I}}/3$ selects out the direction perpendicular to the magnetic field. Therefore, velocity gradients perpendicular to the magnetic field are wiped out by the dot product, whereas velocity gradients parallel to the magnetic field survive to be viscously damped. We are led to conclude that there are no collisions across magnetic field lines, while there are collisions along magnetic field lines. We shall explore this idea more soon; first let us achieve the full set of Braginskii equations by considering the momentum equation.

The momentum equation takes on a similar anisotropy. With the pressure tensor $\vec{P} = p_\perp \vec{\mathbb{I}} + (p_\parallel - p_\perp)\hat{b}\hat{b}$ and the current term $\frac{1}{c}\vec{j} \times \vec{B} = \nabla \cdot \left[B^2/(4\pi)\hat{b}\hat{b} - B^2/(8\pi)\vec{\mathbb{I}} \right]$, we have

$$
mn\frac{D\vec{u}}{Dt} = -\nabla \left(p_\perp + \frac{B^2}{8\pi} \right) + \nabla \cdot \left[\hat{b}\hat{b} \left(p_\perp - p_\parallel + \frac{B^2}{4\pi} \right) \right]
$$

$$
= -\nabla \left(p_\perp + \frac{B^2}{8\pi} \right) + \frac{\vec{B} \cdot \nabla \vec{B}}{4\pi} + \nabla \cdot \left[\left(\hat{b}\hat{b} - \frac{1}{3}\vec{\mathbb{I}} \right) (p_\perp - p_\parallel) \right]
$$

$$
= -\nabla \left(p_\perp + \frac{B^2}{8\pi} \right) + \frac{\vec{B} \cdot \nabla \vec{B}}{4\pi} + \nabla \cdot \left[\frac{3p}{\nu_{coll}} \left(\hat{b}\hat{b} - \frac{1}{3}\vec{\mathbb{I}} \right) \left(\hat{b}\hat{b} - \frac{1}{3}\vec{\mathbb{I}} \right) : \nabla \vec{u} \right]
$$

where the second line uses $p_\perp = p + \frac{1}{3}(p_\perp - p_\parallel)$ and the third uses the Braginskii closure 2.53.

As with the entropy equation, the dot product selects only velocity gradients that are parallel to the magnetic field. It is these motions along field lines that are then subject to viscosity, leading to viscous momentum transport along field lines. On the other hand, Braginskii's ordering 2.44 forbids particles from moving across the field lines more than a distance of a mean free path. The situation is illustrated in Figure ??.

Comparing this result to the non-ideal MHD case with isotropic viscosity, we see that we have achieved viscosity along only the parallel direction whereas the perpendicular direction is still essentially collisionless .

XX do the anisotropic stress tensor here XX

The complete set of equations XX

Extending this closure to the heat flux moment equation leads to anisotropic heat flux along field lines and then an instability due to entropy gradients

known as the MagnetoThermal Instability (MTI), which has been studied both analytically and numerically for its applications to the ICM and winds in hot accretion flows [45, 2, 1, 50, 69, 68, 41, 10]. A similar instability called the Heat-flux-driven Buoyancy Instability is also derived from relaxing the assumption that the magnetic field is perpendicular to temperature gradients [77, 67, 50].

2.5.5 Kinetic effects closure

There are several approaches to modifying the fluid equations to capture kinetic effects. Sharma et al. [89] has studied the transition from collisionless theory to MHD theory and found that the key difference is anisotropic collisions. This same anisotropy was present in the Braginskii MHD equations in the previous section. Braginskii MHD thus seems like an appropriate starting point off of which we can build in additional modifications to attempt to replicate kinetic effects.

Studies of kinetic theory over the years has shown that additional "parasitic" instabilities limit the growth of the pressure anisotropy [91, 52]. The three most important instabilities are the firehose, mirror, and ion cyclotron instabilities. The third will not be reproduced, as in Sharma et al. [91]. It is mostly relevant for plasmas with $\beta \lesssim 100$ whereas the present context of RIAFs has much higher β [94]. The first two instabilities, however, we can look at more closely.

As in outlined in numerous articles, a plasma with the pressure anisotropy

$$p_\perp - p_\parallel < -B^2/4\pi \tag{2.54}$$

is unstable to the firehose instability, and a plasma with pressure anisotropy

$$p_\perp - p_\parallel > B^2/8\pi \tag{2.55}$$

falls prey to the mirror instability [52, 51, 85, 91]. These instabilities are not collisions since the plasma is collisionless. They are rather Alfven waves destabilized by the pressure anisotropy [91]. These waves tangle up the magnetic field of the plasma on the scale of the Larmor radius, which throws particles off of their trajectory. We can therefore model these instabilities as having an effective collision rate and thus a resistivity and viscosity [85, 48].

In light of the thresholds above, we manually cap the pressure anisotropy

over the course of our simulations in Chapter 5. The hope is that such an anisotropy maximum will sufficiently capture the kinetic instabilities in a fluid closure, as discussed in Chapter 5.

Chapter 3

Astrophysics: Context and Background

The accretion disks around supermassive black holes are often (but not always) weakly collisional, hence providing an excellent context for exploring the validity of approximating kinetic theory with a fluid closure. However, the literature on the topic of black hole accretion disks is vast, and so this chapter seeks to extract the important ideas and clarify common jargon in the field.

The chapter will begin by motivating the selection of accretion disks (specifically, radiatively-inefficient accretion flows, RIAFs) in Section 3.1, which also explains some of the observational difficulties involved in seeing accretion disks. An overview of properties of these RIAFs is given in the next section (3.2), followed by important mechanics of accretion disks (Section 3.3) and a brief history of the puzzle that accretion has historically posed (Section 3.4). This section leads into the next chapter, whose focus will be to explain the mechanism behind accretion itself both analytically and through numerical simulations, hence introducing important concepts for Chapter 5.

3.1   Observations of Accretion Disks

With the advent of increasingly high-resolution telescopes and interferometry networks, it is possible to probe structures on the order of the event horizons of supermassive black holes [20]. This is exciting for a number of reasons, the foremost related to this thesis being that direct observations allows for different models to be tested.

An interesting application of these observations is as a test of general relativity through comparisons of the black hole "shadow" measurements and theoretical predictions [75, 58]. However, evaluation of black hole shadow measurements requires simulating the disk around the black hole in order to understand where all the radiation is coming from; currently, GRMHD simulations are used [75]. As mentioned in the Introduction, such models assume the validity of a fluid closure. However, as we will see below, evidence for the low luminosity of certain black holes is strong, suggesting a weakly collisional origin and hence a kinetic model. Thus the main goal of this thesis to evaluate the validity of such simulations has applications even to tests of general relativity.

Direct observations of accretion disks have long been difficult, in part due to technology but also the nature of having a thin accretion disk who emission spectra are not exactly known theoretically. Using both the Event Horizon Telescope and Chandra, we see both radio and millimeter emission from the black hole at the center of our galaxy, Sagittarius A*, which implies both synchrotron radiation (radio) and bremsstrahlung (X-ray). There might also be some anti-Comptonization [65]. However, the Milky way also produces radio emission that obscures Sagittarius A*'s signature. There are also potentially other unknowns, such as jets [58], and the fact that electrons dominate the spectra and whose acceleration and heat transport are precisely what we do not know how to model also presents issues [12]. Progress has been made with GRMHD simulations, like assuming simplified emission models and ruling out a strong funnel emission model [12]. Others have assumed a model (that Sagittarius A* is a RIAF) and come up with parameters such as its spin orientation and magnitude and aspect ratio [7, 8, 19]. However, these fits have massive uncertainties. Other black holes such as M87 and GX 339-4 are also being studied but suffer from poor resolution [74, 56].

XXX explain buckets of energy. XX why riafs (also bh xray binaries: quiescent RIAF to cold black-body when mass accretion rate increase: Das2013),

3.2   Properties of Hot Accretion Flows

Accretion flows are generally characterized by their temperature, their radiative efficiency, and/or their thickness. These types and the relationships

among them will be clarified and discussed soon enough: we first note briefly
that accretion does not have to lead to the formation of a disk. Indeed, some
of the earliest studies on accretion concerned matter falling in radially and
uniformly from all directions onto a compact object: spherical accretion [**?**
]. However, such accretion flows are unlikely to occur in nature because
matter will almost always be rotating with respect to the compact object
and hence have angular momentum.

Hot accretion flows have been discussed in numerous reviews. Here, we
draw from Yuan and Narayan [112].

The term "hot accretion flow" immediately implies a key feature of hot
accretion flows and thereby RIAFs: they are hot. Although temperature
estimates are complicated by not knowing how radiation is vertically trans-
ported [4], we generally know that their temperatures are close to the virial
temperature of the gas. High temperatures produce pressure that counter-
balances gravity and produces a thick disk: RIAFs usually have a ratio of
radius to disk height of about two. These flows also tend to have a much
lower accretion rate than thin disks, leading to a short optical depth and a
non-blackbody spectrum. As mentioned before, the emission of these objects
tends to be due to bremsstrahlung and synchrotron radiation.

3.3   Mechanics of Accretion Disks

This section presents a series of calculations pertaining to important ele-
ments of accretion disks. The issue of the mechanism behind accretion itself
is actually somewhat thorny and was under discussion for a long time, so we
begin by assuming that the disk already exists and look at how such a disk
functions. Accretion itself will be discussed in Section 3.4 and explained
more thoroughly in Chapter 4.

3.3.1   Differential Rotation

Accretion disks are almost always taken to be rotationally-supported. This
means that the centrifugal acceleration balances out gravity and we can
write

$$\frac{GMm}{R^2} = m\Omega^2 R$$

where M is the mass of the black hole, m is the mass of a particle at radius R, and Ω is the rotation speed at radius R. This leads to a Keplerian rotation profile

$$\Omega = \left(\frac{GM}{R^3}\right)^{1/2} \tag{3.1}$$

This equation clearly neglects all other forces except for gravity. This assumption is not always a good one, however. Magnetic fields can quickly grow in these accretion disks, leading to non-Keplerian rotation profiles [83]. For our purposes however, the approximation will hold well enough.

3.3.2 Eddington Luminosity

Radiation from a compact object generates a radiation pressure that begins to counter the gravitational force from the central object. When the luminosity is high enough, the object's gravity is no longer enough to keep it together. When the radiation pressure and gravity exactly cancel, the system is in equilibrium. We can derive the value of the luminosity at this equilibrium, the "Eddington luminosity" or "Eddington limit" as follows (following Spruit [99]):

Assume the radiation has a flux F_{rad} and an opacity, or scattering cross-section times mass, of κ (for ionized hydrogen, $\kappa = \sigma_T/m_p$ where m_p is the mass of the proton and σ_T is the Thomson scattering cross-section of the electron). Then the force balance is given by:

$$\nabla\Phi = \frac{\kappa}{c}F_{\text{rad}} \tag{3.2}$$

The luminosity is defined as the total energy output per time, so we can get it from the flux (amount of light per area per time) by integrating over a surface, which we assume to be spherical:

$$L = \int_S F_{\text{rad}} \cdot dS = \frac{c}{\kappa}\int_S \nabla\Phi \tag{3.3}$$

$$= \frac{c}{\kappa}\int_V \nabla^2\Phi = \frac{4\pi Gc}{\kappa}\int_V \rho dV \tag{3.4}$$

$$= \frac{4\pi GMc}{\kappa} \tag{3.5}$$

Note that the force balance equation does not include any forces other than pressure-gravity equilibrium and the radiation pressure; magnetic forces, for example, are excluded.

In numbers, the Eddington luminosity is given by:

$$L_E = 1.3x10^{38}\frac{M}{M_\odot} \text{ ergs s}^{-1} \tag{3.6}$$

where $M_\odot = 1.989x10^{33}$ g is the mass of the sun. In comparison, the total luminosity of the sun is on the order of 10^{33} ergs s^{-1} [4].

Black holes can exceed the Eddington luminosity because the energy contained in the infalling matter does not have to be radiated; it can simply be swallowed by the black hole and increase its mass. At high accretion rates, radiation could become trapped by the flow and advect into the black hole. This could lead to low observed luminosity.

XX Bondi radius estimate XX

3.3.3 Disk Scale Height

The scale height of a disk is a useful scale for defining distances. It comes from considering a stratified disk; that is, one that has a component of gravity in the vertical direction. As Figure **??** illustrates, the gravitational force in the vertical direction is proportional to the force along the purely horizontal ("R") direction and the ratio of the distances:

$$\frac{F_{gR}}{F_{gz}} = \frac{R}{z} \tag{3.7}$$

Introducing the Keplerian rotation speed $\Omega^2 = GM/R^3$, we have

$$F_{gz} = F_{gR}\frac{z}{R} = \frac{GM}{R^2}\frac{z}{R}$$
$$= \Omega^2 z$$

Now relate F_{gz} to the disk density by considering the force balance equation for equilibrium in the vertical direction:

$$-\frac{1}{\rho}\frac{dP}{dz} = F_{gz}$$

Assuming an isothermal equation of state $P = \rho c^2$, this equation can be integrated:

$$-\frac{1}{\rho}c^2\frac{d\rho}{dz} = F_{gz} = \Omega^2 z$$
$$\rho(z) = \rho_0 e^{-\frac{\Omega^2}{c^2}\frac{z^2}{2}} = \rho_0 e^{-\frac{z^2}{2H^2}}$$

where $H^2 \equiv \frac{c^2}{\Omega^2}$. H can thus be interpreted as the distance a sound wave travels in a shear time (i.e., one rotation). Generally the thickness of a disk is taken to be $2H$. As will be discussed in Section 4, it is often convenient to choose units such that $H = 1$, resulting in numerical domains with dimensions of $(H, 4H, H)$.

3.3.4   Rayleigh Stability Criterion

In hydrodynamics, disks with a Keplerian velocity profile are stable against perturbations. This is intuitively obvious by noting that the Earth does not fall into the sun; that is, circular orbits are stable. Section **??** explores this idea more rigorously, leading to the result that disks with a rotation profile such that

$$\kappa^2 = \frac{1}{R^3} \frac{d(R^4 \Omega^2)}{dR} \geq 0 \qquad (3.8)$$

are stable. This means that specific angular momentum should increase outward for linear stability [4].

3.4   Early Problems in Accretion

The above sections have not addressed how accretion actually works on a fundamental level. So what exactly is accretion?

Accretion is the outward transport of angular momentum, which means that particles that lose angular momentum drop closer to the central accreting object (in the case of this thesis, a black hole) in accordance with differential rotation (Section 3.3.1). The cause of this angular moment transport is the real issue. It seems natural to explain this slowing down via friction; in an accretion disk (or torus), the matter at different radii are not moving at the same velocity (i.e. there is a shear) and hence one might think that there is a sort of coefficient of kinetic friction between particles that slows down their movement and causes them to accrete. The idea that this "molecular" or "shear" viscosity could explain accretion rates is tempting, but in reality is not supported by simulations or observations.

Early simulations solving the MHD equations for a disk as well as observations showed accretion rates on the order of $10^{15} cm^2/s$; however, the standard values of molecular viscosity are in the tens of cm^2/s, somewhere around 14 orders of magnitude too small [99]. This fantastic difference between theory and simulations resulted in several new ideas for explaining

the transport of angular momentum and led to the formulation of one of the most well-known models for thin disks–the α-disk.

The seminal paper of Shakura and Sunyaev [87] explores accretion disks in the context of a binary star system. It essentially characterizes ignorance in the accretion rate via the parameter α, defining the tangential stress $w_{r\phi} = \alpha \rho v_s^2$, where v_s is the sound speed such that $\rho v_s^2 / 2$ is the disk matter's thermal energy density, although definitions vary to order unity across sources [87]. This formulation temporarily removed the need to explain the source of the viscosity and provides a parameter that is easy to tweak in numerical simulations. Although the original paper takes α as a constant for simplicity, it is generally a function of radius. The relevance of the α parameter is apparent even today, as it is a simple way to gain intuition in accretion problems despite its debated value [72].

Despite its intuitive usefulness, the α prescription offers no mechanism for the transport of angular momentum. It was proposed that, while pure molecular viscosity could not explain the observed accretion rates, an "effective" viscosity due to eddy interaction could do the job [4]. In other words, turbulence would generate eddies whose interactions would manifest similar to a viscosity. The problem became to find the source of the turbulence that would lead to outward angular momentum transport. This question is the subject of the next section.

3.4.1 Potential Sources of Turbulence

Supposing that an effective viscosity generated by turbulence can explain observed and simulated accretion rates, the question becomes: what causes this turbulence?

Some, influenced by laboratory fluid mechanics, believed that the sheer property of having a high Reynolds number (the product of a characteristic velocity and length scale divided by the viscosity; huge in astrophysical flows due to the large length scales involved) satisfactorily accounted for the needed turbulence. The mechanism at hand is called "vortex stretching": due to vortex conservation, the stretching of vortices in a shear flow increases the circulation velocity around the vortex tube. This allows for free energy to be extracted from the shear flow [4].

Others, however, suspected that, at least in accretion disks, the flow was fun-

damentally different than those shear flows explored in the aforementioned fluid mechanics labs. Indeed, as demonstrated nicely in [4] and mentioned in Appendix ??, Keplerian flows are stable against perturbations (i.e. experience no turbulence) where shear flows are not (given the Rayleigh stability criterion of Appendix ?? is satisfied). The difference is due to epicycles in Keplerian flows, which sink the energy that would otherwise devolve into prominent disturbances. A high Reynolds number is not enough to explain the necessary turbulence.

It was long thought (and indeed, is still under discussion) that hydrodynamic instabilities could lead to turbulence in accretion disks. One such idea proposed by Paczynski [66] in very flat disks was that gravitational instabilities similar to the Jeans instability could lead to internal heating which would in turn limit the development of the instability, maintaining a somewhat unstable state. While the paper raised important questions concerning heat transport, the effect of the instability is small in hot disks [99].

Convective instabilities have garnered the most interest in terms of generating hydrodynamic turbulence. After all, the Schwarzschild condition (decreasing entropy gradient)...XXXXXXXx

If the mechanism for producing turbulence were global, its effect would not be captured by a local viscosity parameter. [99] mentions several possibilities for generating turbulence this way, including waves and shocks created by tidal forces. These effects can produce accretion at rates up to $\alpha = .01$, but only in hot disks. Global disk winds, of the type suggested by Blandford and Znajek [6], could also transport angular momentum. These magnetically-driven winds could theoretically sweep matter around in such a way as to account for the high accretion rates without a viscosity while also helping account for AGN jets [42]; however, the presence of these winds in all accretion disks is debated. A more universal and fundamental explanation seems more likely.

Magnetic fields were thought to serve an amplifying role in turbulence transport. That is, with pre-existing turbulence, magnetic fields would tangle and speed along the transportation of magnetic fields [87]. It was thought that the magnetic pressure and pressure due to turbulence were distinct, and that magnetic pressure would be insignificant in disk situations, or would require large magnetic fields on the order of $10^7 - 10^8$ G to balance the gravitational pressure of infalling gas [4]. The magnetic field was mainly

considered to be important due to consequences of cyclotron radiation as a cooling mechanism [88]. It was not until the early 1990s that the full significance of magnetic fields was appreciated.

In 1991, Balbus and Hawley [5, 36, 31] closed the conceptual circle by showing that turbulence resulted directly from a weak magnetic field. Pre-existing turbulence was not needed; the entire sequence of generating turbulence and transporting turbulence and angular momentum could be derived as a result of a linear instability in the MHD equations (see Section 4.1). Numerous numerical simulations have since confirmed the important role of magnetic fields in accretion processes. The next chapter will give an overview of the theory of the MRI in ideal and non-ideal MHD in preparation for the comparison between Braginskii MHD and kinetic theory in Chapter 5.

Chapter 4

Computational Context Through the MRI

This chapter examines the solution to the problem of accretion mentioned in the last section of Chapter 3: the MagnetoRotational Instability (MRI). In doing so, it also presents intuition on how the magnetic field interacts in a rotating flow and how the MHD equations outlined in Chapter 2 actually manifest. Although some traction can be gained analytically (indeed, the instability itself arises from linear theory), this chapter will use simulations to illustrate the linear and nonlinear theory of the MRI and to introduce principles of using numerical simulations.

The MRI is fundamentally a local instability; as such, we will zoom in closely to look at a small patch of the overall accretion disk and examine the microphysics at work (see Figure 4.1). The local MHD equations as well as important characteristics such as which wavelengths grow the fastest (and how fast they grow) is outlined in Section 4.1. Non-ideal theory and simulations introduce important concepts such as numerical dissipation in Section 4.2.

4.1   Local Ideal MHD Theory and Simulations

In the local approximation, we consider an unperturbed patch of accretion disk with a Keplerian rotation profile at radius r_0 threaded by a uniform vertical magnetic field. On such small scales, the patch looks like a cube. We can write the equations in Cartesian form with the radial direction as x and the azimuthal direction as y. The Keplerian differential rotation in
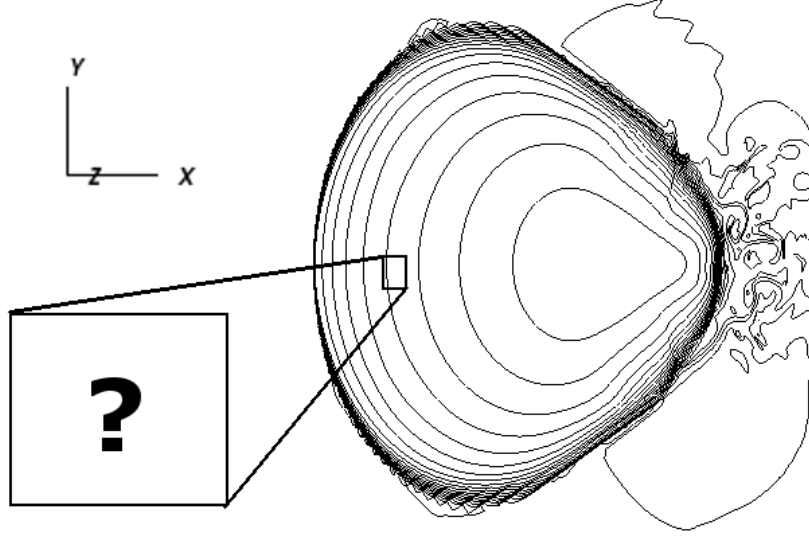
Figure 4.1: Global axisymmetric simulation of a hot accretion flow. Such simulations are expensive, so we zoom in to a small box (the "shearing box", see Section 4.1.4) to look at the microphysics.

this frame looks like a combination of background shear $\vec{u}_0 = 2A_0 x \hat{y}$ where $A_0 = -3\Omega_0/4$ for Keplerian flow as discussed in Chapter 3. The ideal MHD equations in this frame are:

$$\nabla \cdot \vec{u} = \nabla \cdot \vec{B} = 0 \tag{4.1}$$

$$\frac{\partial \vec{u}}{\partial t} = -\vec{u} \cdot \nabla \vec{u} - \frac{1}{\rho} \nabla P + \frac{1}{c\rho} \vec{J} \times \vec{B} - 2\Omega_0 \hat{z} \times \vec{u} - 4A_0 \Omega_0 x \hat{x} \tag{4.2}$$

$$\frac{\partial B}{\partial t} = \nabla \times \left(\vec{u} \times \vec{B} \right) \tag{4.3}$$

The second equation incorporates the Coriolis force $-2\Omega_0 \hat{z} \times \vec{u}$ and the background linear shear [43].

The ultimate goal here is to obtain a relationship between the frequency ω of a wave perturbation and its wavelength k. As such, we consider leading order plane-wave solutions (WKB disturbances) of the form

$$\vec{u} = 2A_0 x \hat{y} + \delta \vec{u} e^{-i(\omega t - kz)} \tag{4.4}$$

$$\vec{B} = B_0 \hat{z} + \delta \vec{B} e^{-i(\omega t - kz)} \tag{4.5}$$

This form of linear theory is the corner stone of linear instability analysis in plasma physics [43, 4, 5, 77]. Plugging in this form and eliminating variables, we attain the dispersion relation

$$\omega^4 - \omega^2[\kappa^2 + 2(\vec{k} \cdot \vec{v}_A)^2] + (\vec{k} \cdot \vec{v}_A)^2 \left((\vec{k} \cdot \vec{v}_A)^2 + \frac{d\Omega^2}{d \ln R} \right) \qquad (4.6)$$

where $\vec{v}_A = \vec{B}/\sqrt{4\pi\rho}$ is the Alfven velocity. This equation is also in the Boussinesq limit that the sound speed goes to infinity, which filters out unimportant sound waves [4, 44]. This schematic derivation is done more rigorously in the appendix (**??**) and a number of sources [4, 5, 36, 31].

4.1.1 Ideal MRI Condition for Stability

From the dispersion relation Eq. 4.6, we can see the condition for stability (that is, real frequency) is

$$(\vec{k} \cdot \vec{v}_A)^2 > -\frac{d\Omega^2}{d \ln R} \qquad (4.7)$$

It is interesting to note that it is always possible to find a wavenumber k such that the system is unstable unless $\frac{d\Omega^2}{d \ln R} > 0$, which would be very uncommon in astrophysical disks [4]. Thus the MRI is always present in weakly magnetized disks with a Keplerian rotation profile.

Also note that if the magnetic field $B = 0$, then the Alfven velocity is also zero and Eq. **??** would have us believe that the hydrodynamic criterion for disk stability is $\frac{d\Omega^2}{d \ln R} > 0$. We know however that the Rayleigh linear stability criterion $\kappa^2 > 0$ says that $4\Omega^2 + \frac{d\Omega^2}{d \ln R} > 0$. The disagreement is due to the assumptions made in using the MHD equations, namely, that the mean free path of particles was much less than the length scales of interest. As k increases, we get down to such small scales that the scales of interest become comparable to the mean free path and thus this assumption is no longer valid. The conflict must be resolved through kinetic theory. This is another incentive to see if we can get the MHD equations to somehow approximate kinetic theory in Chapter **??**.

4.1.2 Ideal MRI Maximum Growth Rate

One of the most important questions for simulations is making sure that the wavelengths that are growing the fastest are resolved on the numerical grid. For this we need the wavelength of the fastest-growing mode.

The maximum unstable growth rate is given by taking the derivative of the dispersion relation with respect to frequency. From this we find that the largest growth rate ω_{max} is given by

$$|\omega_{max}| = \frac{1}{2}\left|\frac{d\Omega}{d\ln R}\right| = \frac{3}{4}\Omega \qquad (4.8)$$

with the Keplerian values on the right. Plugging this back into the dispersion relation shows that the maximimum growth rate occurs when

$$(\vec{k}\cdot\vec{v}_A)^2_{max} = -\left(\frac{1}{4} + \frac{\kappa^2}{16\Omega^2}\right)\frac{d\Omega^2}{d\ln R} = \frac{\sqrt{15}}{4}\Omega \qquad (4.9)$$

There are several interesting things to note here. First, the maximum growth rate is independent of the magnetic field strength. It is also very large and apparently can grow without bound (although as we will show in Section **??**, other instabilities keep it in check). In fact, Balbus and Hawley [3] suggest that this growth rate is the fastest possible for a linear instability that is powered by the free energy of differential rotation.

We can see this growth in action by examining Figure 4.2, which plots perturbations in azimuthal angular momentum. There is clearly a periodic structure which in the x-direction has a wavelength of about half of the box size. This is what we expect from Eq. 4.9:

$$(\vec{k}_{max}\cdot\vec{v}_A)^2 = k^2_{max}\frac{B^2}{4\pi\rho} = \frac{k^2_{max}}{4\pi\rho}\frac{8\pi P}{\beta} = \frac{2P}{\beta\rho}k^2_{max}$$
$$= \frac{15}{16}\Omega^2$$

With the parameters of the simulation having been chosen to set $\Omega = 1$, $P/\rho = 1$, and $\beta = 400$, we have $k_{max} = 13.7\ H^{-1}$ in units of the box size H. The wavelength λ_{max} of the fastest growing mode is then $\lambda_{max} = 2\pi/k_{max} = .46H$. The figure shows this and its orientation along the x-direction. The z-direction mode has a different growth rate and wavelength. In this simulation, the magnetic field is given as $\vec{B} = B_0\sin\left(\frac{x}{H}\right)\hat{z}$. This choice is significant only in that it has zero net flux; the actual form as a sine wave is somewhat arbitrary as it is just a simple way to achieve the zero net flux condition.

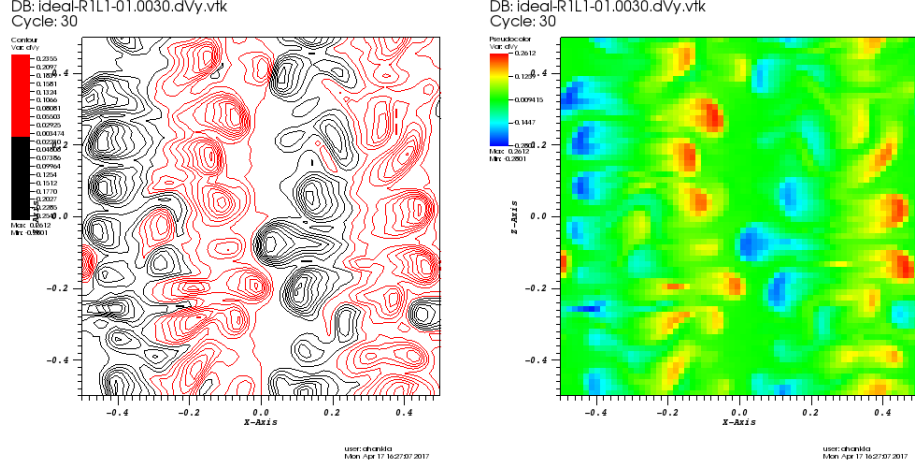More detailed analysis of the instability can be found in Balbus, Steven;

Figure 4.2: Slice at $t = 3.0$ orbits. Central body is on the left; z-direction is up. Left: Contour plot of angular momentum perturbations. Black is a perturbation in the negative y-direction, while red is in the positive y-direction. XX do this XX. Right: Pseudocolor plot of angular momentum perturbations. Plot is normalized to XX do this XX. The growth of the x-direction mode with wavelength .5H is clear.
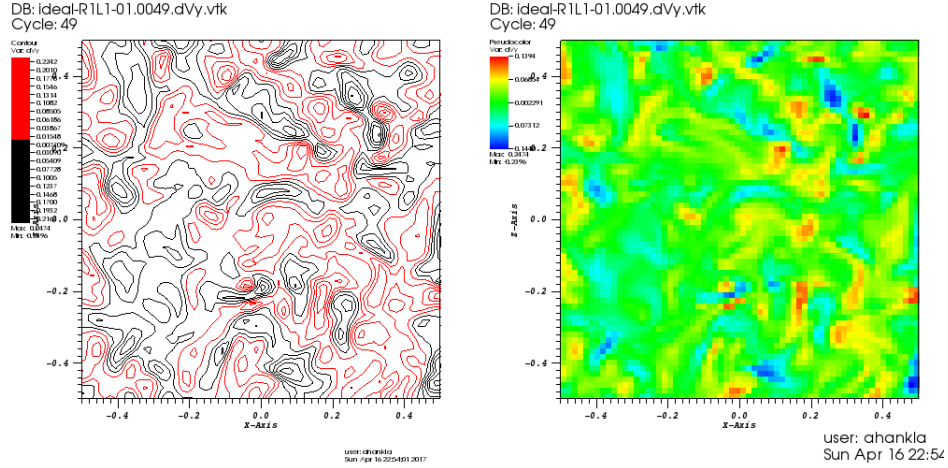

Figure 4.3: Slice at $t = 4.9$ orbits of angular momentum perturbations with same description as Fig. 4.2. The system has proceeded to the nonlinear turbulence phase as evidenced by the lack of structure.

Hawley [5] and Balbus and Hawley [4]. The instability is different given different initial configurations of the magnetic field, the most important being the aforementioned zero net-flux condition. A radial magnetic field component will yield a time dependent azimuthal magnetic field component; however, this dependency does not really affect the MRI evolution because the axisymmetric instability is independent of B_ϕ [4].

We can see that the MRI is working because over time the magnetic energy and kinetic energy increase, shown in Figure 4.4. Some of the (in this case, unlimited) energy from differential rotation is going into turbulence, sustaining the magnetic field and churning around particles (hence increasing their kinetic energy). The linear phase of the MRI in Figure 4.2 gives way to turbulence shortly thereafter, as shown in Figure 4.3. The nonlinear regime is the steady-state solution and is what we are most interested in for this thesis. This is the regime that is difficult to describe analytically. Note that references such as Balbus, Steven; Hawley [5] that perform two-dimensional calculations see the rise of a "channel mode" between the linear and nonlinear evolution. In three-dimensional calculations the channel mode is harder to see because it breaks down much faster into turbulence [33, 32].

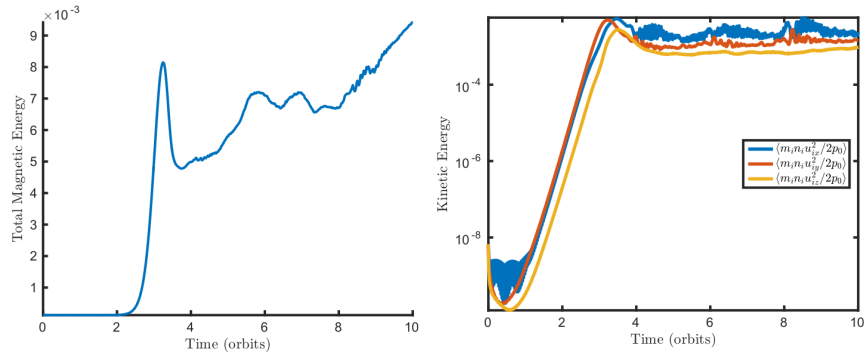Details of the method used to produce Figures 4.2 and 4.4 are explained in Section 4.1.4.

Figure 4.4: Left: Magnetic energy increases due to MRI turbulence. Total magnetic energy has been normalized to initial pressure. Right: Kinetic energy, also normalized to initial pressure. The large bump around $t = 3$ orbits is due to the channel mode (see text). Resolution is $(64, 128, 64)$ zones for the $(H, 4H, H)$ box.
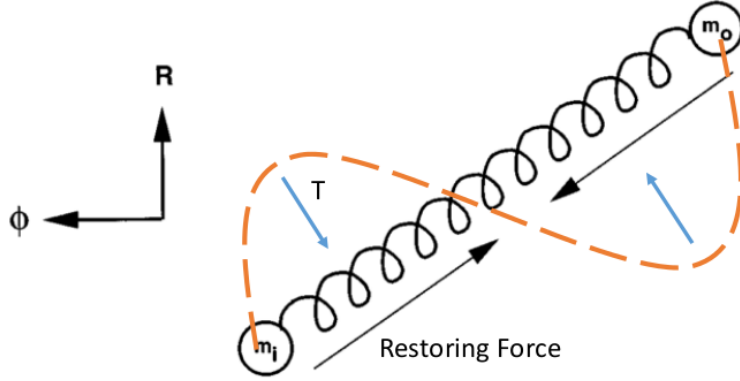
Figure 4.5: Illustration of the MRI with the magnetic tension T working in the same way as the restoring force of a spring. Adapted from Balbus and Hawley [4].

4.1.3 Spring Interpretation

It turns out that the local equations are also those of two orbiting masses coupled by a spring. A more complete derivation is given in Appendix **??** and Balbus and Hawley [4], so here we only provide the physical intuition for how the MRI leads to accretion.

The situation is illustrated in Figure 4.5. One mass (call it m_o) is orbiting at a slightly higher-radius orbit r_o thanks to a perturbation. Due to the Keplerian rotation law, this mass orbits slower than the mass m_i at lower radius r_i. This means that m_i pulls ahead of m_o, thus stretching the spring. Hooke's law exerts a force pulling the springs back together, causing the inner mass to lose angular momentum and the outer mass to gain angular momentum. This means that m_i drops down to a lower orbit while m_o pulls away, thereby stretching the spring even more. The process runs away and m_i falls inward while m_o falls outward, producing outward angular momentum transport.

Obviously there is not an actual spring connecting the two masses. The job of the spring's restoring force is done by magnetic tension $\left(\frac{1}{4\pi} (\vec{B} \cdot \nabla) \vec{B} \right)$, which tries to unfurl magnetic field lines. The magnetic field is perturbed when the fluid elements are due to the flux-freezing explained earlier. The field line is drawn as a dotted orange line in Figure 4.5.

4.1.4 Shearing Box Method

Simulations of the MRI are often achieved by solving the Cartesian set of MHD equations described above with periodic boundary conditions. The model's linear shear means that if a particle moves outward with radius, it also moves azimuthally. The boundary conditions for a function f are expressed as

$$f(x, y, z) = f(x + H_x, y + \frac{3}{2}\Omega_0 H_x t, z) \qquad (4.10)$$

$$f(x, y, z) = f(x, y + H_y, z) \qquad (4.11)$$

$$f(x, y, z) = f(x, y, z + H_z) \qquad (4.12)$$

where the first line is for the x boundary, the second for the y boundary, and the third for the z boundary. The size of the computational regime is H_x in the x-direction, H_y in the y-direction, and H_z in the z-direction. In these equations the shear has been Taylor-expanded about the relative velocity $w_y = v_y - R\Omega_0 = R(\Omega - \Omega_0) \sim x \left(R\frac{d\Omega}{dR}\right)_0 = -\frac{3}{2}\Omega_0 x$ for a Keplerian disk. These boundary conditions are visually explained in Figure 4.6. More details can be found in Balbus and Hawley [4] or in the first paper simulating the MRI [31].

Since the box is in the local approximation, we can take the density and pressure to be initially constant. In this thesis, we evolve the system adiabatically (Eq. **??**), as opposed to isothermally ($P = \rho c^2$, where c is the sound speed). We also choose units such that the fiducial angular velocity of the shearing box as it goes around the central body is 1: $\Omega_0 = 1$. Also choosing $P = \rho = 1$, we have that the sound speed $c = 1$ and thus that the disk height (introduced in Section **??**) $H = 1$.

Finally, note the importance of resolution: if the fastest growing MRI mode is smaller than the size of each zone, then the simulation will not resolve the mode and the set-up will appear stable. Calling the size of each zone $(\Delta x, \Delta y, \Delta z)$, the smallest resolvable wavelength in the x-direction is

$$\lambda_{min} = 2\Delta x$$

With a resolution of 64 zones per scale height H (the size of the entire computational regime), each zone has a size $\Delta x = 1/64$ $[H]$ so the smallest wavelength we can see corresponds to $\lambda_{min} = 1/32$ $[H] \approx .03$ $[H]$. We need the fastest growing wavelength to be bigger than this in order to see

turbulence. This sets a limit on what β can be. We know that the fastest growing wavelength is

$$\frac{15}{16}\Omega^2 = k_{fast}^2 v_A^2 = \frac{2}{\beta}\frac{(2\pi)^2}{\lambda_{fast}^2}$$

$$\lambda_{fast}^2 = \frac{32(2\pi)^2}{15\beta}$$

Requiring that $\lambda_{fast} \geq \lambda_{min}$ yields an upper limit on β, which luckily is in the 10^4 range and thus well above the $\beta = 400$ case we are considering. Thus in the figures above, we are resolving the fastest-growing wavelength.
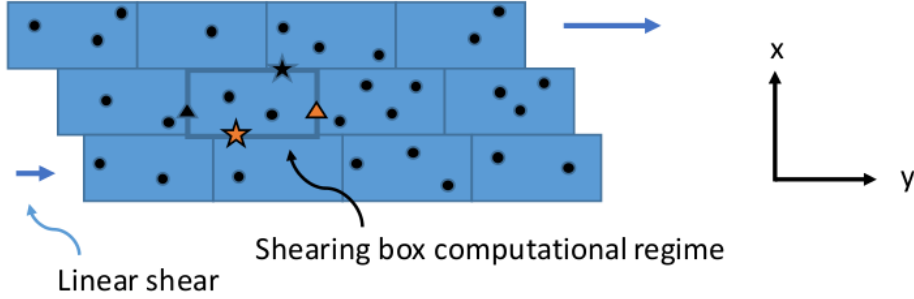

Figure 4.6: Illustration of the shearing box method. The computational regime itself is outlined in thick blue ("shearing box computational regime") and has dimensions of $H_x = H$, $H_y = 4H$, and $H_z = H$ (z dimension not shown). The azimuthal direction needs a larger computational domain because the shear stretches the modes out. The linear shear $\vec{u}_0 = 2A_0 x\hat{y}$ is illustrated by arrows that vary in size with the x-location. The boundary conditions of Eqns. 4.10-4.12 are shown by the orange and black triangle and star. A particle that travels off the right (y) boundary (orange triangle) reappears on the left y boundary at the same x-position, represented by the black triangle. The x boundary condition takes into account the linear shear, such that the orange star leaving through the x boundary reappars displaced as though by a shear at the top of the regime (black star). Adapted from Balbus and Hawley [4].

4.2 Local Non-ideal MHD Theory and Simulations

This section is particularly relevant for the next chapter and understanding the effects of changing resistivity and viscosity in a fluid model. When we introduce non-ideal MHD components such as resistivity and viscosity, the resolution of simulations becomes even more important. This is because certain length scales are damped faster than others. A problem in the literature involving the lack of convergence for zero net-flux simulations such as these was recently resolved [25, 95].

As a rough estimate, resistivity has a characteristic wavelength $k^2\eta \sim \Omega$ that is damped by $1/e$ over the time it takes for a sound wave to traverse the disk. Too big a value will damp the MRI and stabilize the disk [23]. Viscosity similarly damps wave numbers $k^2\nu \sim \Omega$. The balance between these two competing scales means that there is a limited parameter space in magnetic Prandtl number that can be explored. Fromang et al. [26] for example found that the magnetic Prandtl number needs to be greater than 4 in order to sustain turbulence, an issue also addressed by Simon et al. [98] (the case is different for net-flux simulations [97]). This issue was confirmed across several different code suites Fromang et al. [26]. The growth rate of resistive MHD is examined more rigorously in Balbus and Hawley [4].

However, the magnetic Reynolds number is also important, since if it is too small then numerical dissipation will dominate over physical dissipation and the magnetic Prandtl number will mean nothing. To figure out what regimes of the transport coefficients η and ν to look at, we must find values that are both physically meaningful and that do not overdamp the fastest growing modes (which would lead to stability).

We begin by requiring that the smallest resolvable wavelength be damped by physical resistivity: this sets

$$\eta \sim \frac{\lambda_{min}^2 \Omega}{(2\pi)^2} \gtrsim \frac{(1/32)^2}{(2\pi)^2} = 2.5e - 5$$

For good measure we will take $\eta = 1e - 4$ or above in our simulations. Also note that the value of η that corresponds to damping the fastest growing mode is

$$\eta_{fast} = \frac{1}{k_{fast}^2} \approx .005$$

With a resistivity lower than 5e-3 we ensure that the MRI will still be able to grow.

A set of simulations with $\eta = 1e-4$ is shown in Figure ??a) with varying magnetic Prandtl number. We can see that magnetic energy increases with increasing mPrandtl number. However, Figure ??b) shows increasing mPrandtl that does not lead to monotonically. To explain this, look at how the viscosity affects the fastest growing mode. The characteristic viscously damped wavenumber k_ν is

$$k_\nu^2 = \frac{\Omega}{\nu} = \frac{\Omega}{\eta} \frac{\eta}{\nu} = k_\eta^2 \frac{1}{Pm}$$

For $\eta = 1e-4$, we have $k_\eta = 10^2$ and $k_\nu = \frac{1}{2}10^2 = 50$ for $Pm = 4$ or $k_\nu = \frac{1}{4}10^2 = 25$ for $Pm = 16$. However, for $eta = 2e-4$, low mPrandtl such as $Pm = 4$ gives $k_\nu = \frac{1}{\sqrt{8}}10^2 \approx 35$, but higher mPrandlt like $Pm = 16$ gives $k_\nu = \frac{1}{\sqrt{32}}10^2 \approx 17$. The fastest growing mode is $k_{fast} \approx 14$, so for higher resistivities the higher mPrandtl numbers start to significantly damp modes that are most important to the MRI. In such cases, the flow will not be turbulent and so the magnetic energy will decay. A schematic portrayal of the scales involved is shown in Figure 4.8.
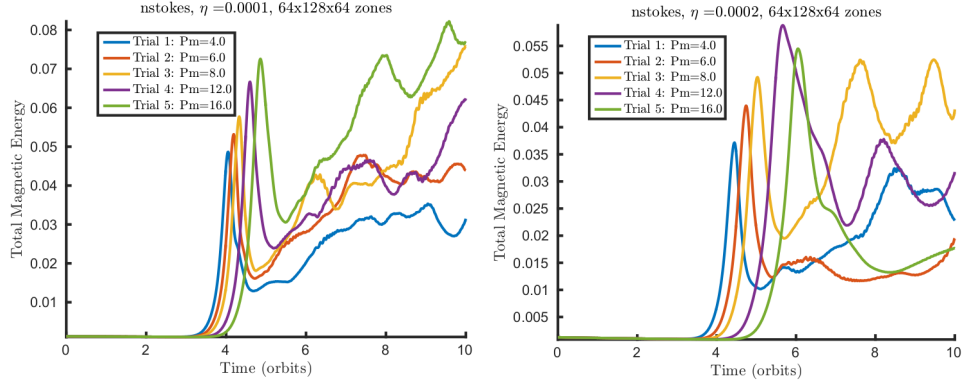
Figure 4.7: Plots of magnetic energy with increasing magnetic Prandlt number. The left panel has $\eta = 1e - 4$ and the right has $\eta = 2e - 4$. For the lower resistivity, magnetic energy increases monotonically up to a magnetic Prandtl number of 16. For a higher resistivity however, viscous damping begins to stabilize the MRI and higher magnetic Prandlt numbers decrease in magnetic energy.
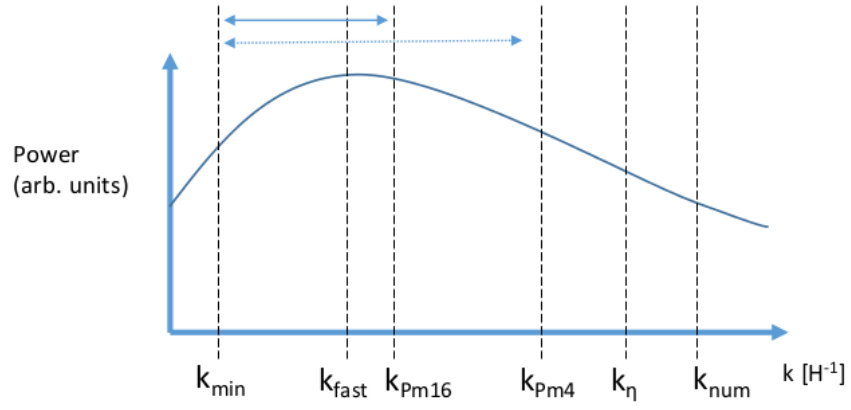
Figure 4.8: Rough illustration of scales involved in a shearing box simulation. The fastest-growing mode is labelled k_{fast}; the lowest resolvable wavenumber has a wavelength twice the disk scale height and is labelled as k_{min}. Numerical dissipation cuts off wavenumbers above k_{num}, while resistivity damps wavenumbers above k_η. Two values for k_ν are shown, one for $Pm = 4$, the other for $Pm = 16$. The lower mPrandtl number resolves a much wider range of wavenumbers than the higher value, as shown by the horizontal arrows. Shape of power spectrum comes from dispersion relation.

Chapter 5

Modified Fluid Closure of a Collisionless Plasma

This chapter puts together the pieces of the previous chapters in order to approximate a collisionless plasma with a modified fluid closure.

5.1 Anisotropic Viscosity

Here, get a sense of what anisotropic viscosity does. This provides a control for the next section where the anisotropy will be capped.

5.2 Pressure Anisotropy Maximum

Following the suggestion by Kunz et al. [52], we implement a maximum pressure anisotropy to mimic the mirror and firehose instabilities. Explained in Section 2.5.5, we reproduce these thresholds here for completeness. The firehose instability threshold is given as

$$p_\perp - p_\parallel < -B^2/4\pi \tag{5.1}$$

and the mirror instability threshold is

$$p_\perp - p_\parallel > B^2/8\pi \tag{5.2}$$

XX Sharma 2008: dispersion relation? predict growth rates?

Bibliography

[1] S. a. Balbus. Convective and Rotational Stability of a Dilute Plasma. *The Astrophysical Journal*, 562(2):909–917, 2001. ISSN 0004-637X. doi: 10.1086/323875. URL `http://arxiv.org/abs/astro-ph/0106283`.

[2] Steven a. Balbus. Stability, Instability, and "Backward" Transport in Stratified Fluids. *The Astrophysical Journal*, 534(1):420–427, 2000. ISSN 0004-637X. doi: 10.1086/308732.

[3] Steven A. Balbus and John F. Hawley. Is the Oort A-value a universal growth rate limit for accretion disk shear instabilities? *Astrophys. J*, 392:662–666, 1992. ISSN 0004-637X. doi: 10.1086/171467.

[4] Steven A Balbus and John F Hawley. Instability, turbulence, and enhanced transport in accretion disks. *Reviews of Modern Physics*, 70(1):1–53, 1998. ISSN 0034-6861. doi: 10.1103/RevModPhys.70.1. URL `http://adsabs.harvard.edu/cgi-bin/nph-data{_}query?bibcode=1998RvMP...70....1B{&}link{_}type=ABSTRACT{%}5Cnpapers://0be24a46-325a-4116-a3c6-fd8a3b614472/Paper/p9932{%}5Cnhttp://link.aps.org/doi/10.1103/RevModPhys.70.1`.

[5] John Balbus, Steven; Hawley. A Powerful Local Shear Instability in Weakly Magnetized Disks I. Linear Analysis. *The Astrophysical Journal*, 376:214–222, 1991.

[6] R.D. Blandford and R. L. Znajek. Electromagnetic extraction of energy from Kerr Black Holes. *Mon. Not. R. astr. Soc.*, 179:433–456, 1977.

[7] Avery E Broderick, Vincent L Fish, Sheperd S Doeleman, and Abraham Loeb. ESTIMATING THE PARAMETERS OF SAGITTARIUS A*'s ACCRETION FLOW VIA MILLIMETER VLBI. *The Astrophysical Journal*, 697:45–54, 2009. doi: 10.1088/0004-637X/697/1/45. URL `http://iopscience.iop.org/article/10.1088/0004-637X/697/1/45/pdf`.

[8] Avery E Broderick, Vincent L Fish, Sheperd S Doeleman, and Abraham Loeb. EVIDENCE FOR LOW BLACK HOLE SPIN AND PHYSICALLY MOTIVATED ACCRETION MODELS FROM MILLIMETER-VLBI OBSERVATIONS OF SAGITTARIUS A*. *The Astrophysical Journal*, 735(15pp), 2011. doi: 10.1088/0004-637X/735/2/110. URL `http://iopscience.iop.org/article/10.1088/0004-637X/735/2/110/pdf`.

[9] Avery E Broderick, Ramesh Narayan, John Kormendy, Eric S Perlman, Marcia J Rieke, and Sheperd S Doeleman. THE EVENT HORIZON OF M87. *The Astrophysical Journal*, 805:179, 2015. doi: 10.1088/0004-637X/805/2/179. URL `http://iopscience.iop.org/article/10.1088/0004-637X/805/2/179/pdf`.

[10] De Fu Bu, Mao Chun Wu, and Ye Fei Yuan. Effects of anisotropic thermal conduction on wind properties in hot accretion flow. *Monthly Notices of the Royal Astronomical Society*, 459(1):746–753, 2016. ISSN 13652966. doi: 10.1093/mnras/stw723.

[11] C L Carilli and G B Taylor. CLUSTER MAGNETIC FIELDS. *Annu. Rev. Astron. Astrophys*, 40:319–48, 2002. doi: 10.1146/annurev.astro.40.060401.093852. URL `http://annualreviews.org/doi/pdf/10.1146/annurev.astro.40.060401.093852`.

[12] Chi-Kwan Chan, Dimitrios Psaltis, Feryaï Ozel, Ramesh Narayan, and Aleksander Adowski. THE POWER OF IMAGING: CONSTRAINING THE PLASMA PROPERTIES OF GRMHD SIMULATIONS USING EHT OBSERVATIONS OF Sgr A *. *The Astrophysical Journal*, 799(114pp), 2015. doi: 10.1088/0004-637X/799/1/1. URL `http://iopscience.iop.org/article/10.1088/0004-637X/799/1/1/pdf`.

[13] Benjamin D Chandran and Timothy J Dennis. CONVECTIVE STABILITY OF GALAXY-CLUSTER PLASMAS. *The Astrophysical Journal*, 642:140–151, 2006.

[14] G. Chew, M. Goldberger, and F. Low. The Boltzmann equation and the one-fluid hydromagnetic equations in the absence of particle collisions. *Proceedings of the Royal Society of London. Series A Mathematical and Physical Sciences*, 236(1204), 1956. URL `www.jstor.org`.

[15] C Courtois, R A D Grundy, A D Ash, D M Chambers, N C WoolseyR O Dendy, K G McClements, N C Woolsey, and R O Dendy. Experiment on collisionless plasma interaction with applications to supernova remnant physics. *Citation: Physics of Plasmas*, 11(3386), 2004. doi: 10.1063/1.1752930. URL `http://dx.doi.org/10.1063/1.1752930http://aip.scitation.org/toc/php/11/7`.

[16] Upasana Das and Prateek Sharma. Radiatively inefficient accretion flow simulations with cooling: implications for black hole transients. *MNRAS*, 435:2431–2444, 2013. doi: 10.1093/mnras/stt1452. URL `https://oup.silverchair-cdn.com/oup/backfile/Content{_}public/Journal/mnras/435/3/10.1093/mnras/stt1452/2/stt1452.pdf?Expires=1489244484{&}Signature=UOdGDsRQU7sqmasAjawlZqXmoWV56t26VdoqVwPhLVdgBnTP4wRMCP6AFVrhVcvR4LeRB9Okugp5oEsC`

[17] Upasana Das and Prateek Sharma. Cooling and black hole disk transitions. *ASI Conference Series*, 8:27–30, 2013.

[18] S. Dean, E. McLean, J. Stamper, and H. Griem. Demonstration of Collisionless Interactions between Interstreaming Ions in a Laser-produced-plasma Experiment. *Physical Review Letters*, 27(8):487–490, 1971. URL `https://journals-aps-org.ezproxy.princeton.edu/prl/pdf/10.1103/PhysRevLett.27.487`.

[19] Jason Dexter and P Chris Fragile. Tilted black hole accretion disc models of Sagittarius A*: time-variable millimetre to near-infrared emission. *MNRAS*, 432:2252–2272, 2013. doi: 10.1093/mnras/stt583. URL `https://oup.silverchair-cdn.com/oup/backfile/Content{_}public/Journal/mnras/432/3/10.1093/mnras/stt583/3/stt583.pdf?Expires=1490824579{&}Signature=eHMpnogDQWMSVkVFaJludDUYoRcFDblIOmCBpJ6tqRu2kpLaTbEn-CouvLXhz16h9Yi6gX4fuavh9Zac`

[20] S Doeleman, Eric Agol, Fred C Baganoff Geoffrey Bower, Avery Broderick Andrew Fabian, Paul Ho Mareki Honma Thomas Krichbaum Avi Loeb Dan Marrone NRAO, U Chicago Mark Reid Alan Rogers, Irwin Shapiro Peter Strittmatter Remo Tilanus Jonathan Weintroub Alan Whitney, and Melvyn Wright. Imaging an Event

Horizon: submm-VLBI of a Super Massive Black Hole. *astro 2010: The Decadal Review Committee*, 2009. URL `https://arxiv.org/ftp/arxiv/papers/0906/0906.3899.pdf`.

[21] A. Fabian. COOLING FLOWS IN CLUSTERS OF GALAX-IES. *Annu. Rev. Astron ASlrophys*, 32:277–318, 1994. URL `http://www.annualreviews.org/doi/pdf/10.1146/annurev.aa.32.090194.001425`.

[22] R.P. Fender, J. Homan, and T.M. Belloni. Jets from black hole X-ray binaries: testing, refining and extending empirical models for the coupling to X-rays. *Mon. Not. R. Astron. Soc.*, 396:1370–1382, 2009.

[23] Timothy P Fleming, James M Stone1, and John F Hawley. THE EFFECT OF RESISTIVITY ON THE NONLINEAR STAGE OF THE MAGNETOROTATIONAL INSTABILITY IN ACCRETION DISKS. *THE ASTROPHYSICAL JOURNAL*, 530:464–477, 2000. URL `http://iopscience.iop.org/article/10.1086/308338/pdf`.

[24] Francois Foucart, Mani Chandra, Charles F. Gammie, and Eliot Quataert. Evolution of accretion discs around a kerr black hole using extended magnetohydrodynamics. *Monthly Notices of the Royal Astronomical Society*, 456(2):1332–1345, 2015. ISSN 13652966. doi: 10.1093/mnras/stv2687.

[25] S Fromang and J Papaloizou. Astrophysics MHD simulations of the magnetorotational instability in a shearing box with zero net flux I . The issue of convergence. *Astronomy and Astrophysics*, 1122:1113–1122, 2007.

[26] S Fromang, J Papaloizou, G Lesur, and T Heinemann. MHD simulations of the magnetorotational instability in a shearing box with zero net flux II. The effect of transport coefficients. *A&A*, 476: 1123–1132, 2007. doi: 10.1051/0004-6361:20077943. URL `http://www.aanda.org/articles/aa/pdf/2007/48/aa7943-07.pdf`.

[27] C. Gammie. Layered Accretion in T Tauri Disks. *The Astrophysical Journal*, 457:355–362, 1996. URL `http://articles.adsabs.harvard.edu/cgi-bin/nph-iarticle{_}query?1996ApJ...457..355G{&}defaultprint=YES{&}filetype=.pdf`.

[28] M L Goldstein, D A Roberts, and W H Matthaeus. MAG-NETOHYDRODYNAMIC TURBULENCE IN THE SOLAR

WINDl. *Annu. Rev. Astron. Astrophys*, 33:283–325, 1995. URL `http://www.annualreviews.org/doi/pdf/10.1146/annurev.aa.33.090195.001435`.

[29] J T Gosling. COROTATING AND TRANSIENT SOLAR WIND FLOWS IN THREE DIMENSIONS. *Annu. Rev. Astron. Astrophys*, 34:35–73, 1996. URL `http://annualreviews.org/doi/pdf/10.1146/annurev.astro.34.1.35`.

[30] G Grieger and I Milch. {D}as {F}usionsexperiment {WENDELSTEIN} 7-{X}. *Physikalische Bl{ä}tter*, 49(11):1001, 1993.

[31] J. Hawley and S. Balbus. A Powerful Local shear instability in weakly magnetized Disks: III. Long-Term evolution in a shearing sheet. *The Astrophysical Journal*, 400:595–609, 1992.

[32] J. Hawley, C. Gammie, and S. Balbus. Local Three-Dimensional Simulations of an accretion disk hydromagnetic dynamo. *The Astrophysical Journal*, 464:690–703, 1996. URL `http://articles.adsabs.harvard.edu/cgi-bin/nph-iarticle{_}query?1996ApJ...464..690H{&}defaultprint=YES{&}filetype=.pdf`.

[33] John F. Hawley, Charles F. Gammie, and Steven a. Balbus. Local Three-dimensional Magnetohydrodynamic Simulations of Accretion Disks. *The Astrophysical Journal*, 440:742, 1995. ISSN 0004-637X. doi: 10.1086/175311.

[34] John F Hawley, Steven A Balbus, and James M Stone. A Magnetohydrodynamic Nonradiative Accretion Flow in Three Dimensions. *The Astrophysical Journal Letters*, 554(1):49–52, 2001. ISSN 0004637X. doi: 10.1086/320931. URL `http://iopscience.iop.org/1538-4357/554/1/L49{%}5Cnpapers2://publication/uuid/2C3A60D4-41E8-4DE1-B690-3CB8AF0B7406{%}5Cnhttp://stacks.iop.org/1538-4357/554/i=1/a=L49`.

[35] John F Hawley, Christian Fendt, Martin Hardcastle, Elena Nokhrina, and Alexander Tchekhovskoy. Disks and Jets Gravity, Rotation and Magnetic Fields. *Space Sci Rev*, 191:441–469, 2015. doi: 10.1007/s11214-015-0174-7. URL `http://download.springer.com/static/pdf/328/art{%}253A10.1007{%}252Fs11214-015-0174-7.pdf?originUrl=`

```
http{%}3A{%}2F{%}2Flink.springer.com{%}2Farticle{%}2F10.
1007{%}2Fs11214-015-0174-7{&}token2=exp=1492185262{~}acl=
{%}2Fstatic{%}2Fpdf{%}2F328{%}2Fart{%}25253A10.
1007{%}25252Fs11214-015-017.
```

[36] Steven Hawley, John; Balbus. A Powerful Local Shear Instability in Weakly Magnetized Disks II. Nonlinear Evolution. *The Astrophysical Journal*, 376:223–233, 1991.

[37] R. D. (Richard D.) Hazeltine and F. Waelbroeck. *The framework of plasma physics*. Perseus Books, Reading, 2004. ISBN 9780813342139.

[38] G Janeschitz, P Barabaschi, G Federici, M Shimada, D J Campbell, V Mukhovatov, R Aymar, V A Chuyanov, M Huguet, and Y Shimomura. Overview of ITER-FEAT -The future international burning plasma experiment The requirements of a next step large steady state tokamak Chapter 1: Overview and summary Overview of ITER-FEAT — The future international burning plasma experiment. *Nucl. Fusion*, 41:1301–1310, 2001. URL `http://iopscience.iop.org/0029-5515/41/10/301`.

[39] Yan-Fei Jiang, James M. Stone, and Shane W. Davis. ON THE THERMAL STABILITY OF RADIATION-DOMINATED ACCRETION DISKS. *The Astrophysical Journal*, 778(1):65, nov 2013. ISSN 0004-637X. doi: 10.1088/0004-637X/778/1/65. URL `http://stacks.iop.org/0004-637X/778/i=1/a=65?key=crossref.bc87bad3230780b5bb248cfade3911a6`.

[40] Yan-Fei Jiang, James M. Stone, and Shane W. Davis. a Global Three-Dimensional Radiation Magneto-Hydrodynamic Simulation of Super-Eddington Accretion Disks. *The Astrophysical Journal*, 796 (2):106, 2014. ISSN 1538-4357. doi: 10.1088/0004-637X/796/2/106. URL `http://stacks.iop.org/0004-637X/796/i=2/a=106?key=crossref.3345a0b680e6eb3d7be5065544be0d95`.

[41] Bryan M. Johnson and Eliot Quataert. The Effects of Thermal Conduction on Radiatively Inefficient Accretion Flows. *The Astrophysical Journal*, 660(2):1273–1281, 2007. ISSN 0004-637X. doi: 10.1086/513065. URL `http://stacks.iop.org/0004-637X/660/i=2/a=1273`.

[42] A. Koenigl. Self-similar models of magnetized accretion disks. *The Astrophysical Journal*, 342:208–223, 1989. URL `http://articles.`

adsabs.harvard.edu/cgi-bin/nph-iarticle{_}query?1989ApJ.
..342..208K{&}defaultprint=YES{&}filetype=.pdf.

[43] M. Kunz. AST 521 Homework 4, 2016.

[44] M. Kunz. Notes on the Boussinesq Approximation, 2016.

[45] M. Kunz. Braginskii-MHD and application to ICM, 2016.

[46] M. Kunz. AST521 Kunz Lecture 1: Kinetic description of a plasma, 2016.

[47] M. Kunz. AST521 Kunz Lecture Non-ideal MHD in poorly ionized plasma.pdf, 2016.

[48] M. Kunz. Private Communication, 2017.

[49] Matthew Kunz. press-Firehose and Mirror Instabilities in a Collisionless Shearing Plasma. 2010.

[50] Matthew W Kunz. Dynamical stability of a thermally stratified intracluster medium with anisotropic momentum and heat transport. *Mon. Not. R. Astron. Soc*, 417:602–616, 2011. doi: 10.1111/j.1365-2966.2011.19303.x. URL `https://oup.silverchair-cdn.com/oup/backfile/Content{_}public/Journal/mnras/417/1/10.1111/j.1365-2966.2011.19303.x/2/mnras0417-0602.pdf?Expires=1492705308{&}Signature=dj6-sZp2Ngrr-6XcmLv4GylnuOueY3I2BCqQ5khkIc{~}Gcw-fGODNXipJlCrGyZ21lqoGRA4334KD7p`

[51] Matthew W Kunz, Alexander A Schekochihin, and James M Stone. Firehose and Mirror Instabilities in a Collisionless Shearing Plasma. *Physical Review Letters*, 112, 2014. doi: 10.1103/PhysRevLett.112.205003. URL `https://journals.aps.org/prl/pdf/10.1103/PhysRevLett.112.205003`.

[52] Matthew W Kunz, James M Stone, and Eliot Quataert. Magnetorotational Turbulence and Dynamo in a Collisionless Plasma. *Physical Review Letters*, 117, 2016. doi: 10.1103/PhysRevLett.117.235101.

[53] G Lesur and P.-Y Longaretti. Impact of dimensionless numbers on the efficiency of magnetorotational instability induced turbulent transport. *Mon. Not. R. Astron. Soc*, 378:1471–1480, 2007. doi: 10.1111/j.1365-2966.2007.11888.x. URL `https://oup.silverchair-cdn.com/oup/backfile/Content{_}public/`

Journal/mnras/378/4/10.1111/j.1365-2966.2007.11888.x/
3/mnras0378-1471.pdf?Expires=1490726134{&}Signature=
ItAaoeYsSoiYKNwbB{~}vtXZgku-OMqnPO21s-g{~}p-u0fgMTTXvLToagk6rZO{~}NwUxkxm5mPZMXW

[54] S M Mahajan and R D Hazeltine. Fluid description of a magne-
tized plasma Fluid description of a magnetized plasma a.... *Ci-
tation: Physics of Plasmas*, 9:1882–1889, 2002. doi: 10.1063/
1.1445178. URL `http://dx.doi.org/10.1063/1.1445178http://`
`aip.scitation.org/toc/php/9/5`.

[55] W. H. Matthaeus and M. L. Goldstein. Measurement of the rugged in-
variants of magnetohydrodynamic turbulence in the solar wind. *Jour-
nal of Geophysical Research*, 87:6011–6028, 1982. ISSN 0148-0227. doi:
10.1029/JA087iA08p06011.

[56] Michael Mccourt and Ann-Marie Madigan. Going with the flow:
using gas clouds to probe the accretion flow feeding Sgr A *.
MNRAS, 455:2187–2199, 2016. doi: 10.1093/mnras/stv2232.
URL `https://oup.silverchair-cdn.com/oup/backfile/`
`Content{_}public/Journal/mnras/455/2/10.1093/mnras/`
`stv2232/2/stv2232.pdf?Expires=1490824057{&}Signature=`
`PgUN{~}CD16kMLRWYk-iCMACXX7VaC0N9FL6rncsPbjmDvAXHs{~}6TDlG-A4USQjXUDfoAMFajWVQq6`

[57] P J Mendygral, T W Jones, and K Dolag. MHD SIMULATIONS OF
ACTIVE GALACTIC NUCLEUS JETS IN A DYNAMIC GALAXY
CLUSTER MEDIUM. *The Astrophysical Journal*, 750(17pp), 2012.
doi: 10.1088/0004-637X/750/2/166. URL `http://iopscience.iop.`
`org/article/10.1088/0004-637X/750/2/166/pdf`.

[58] Monika Moscibrodzka, Heino Falcke, Hotaka Shiokawa, and Charles F.
Gammie. Observational appearance of inefficient accretion flows
and jets in 3D GRMHD simulations: Application to Sagittarius
A*. *Astronomy and Astrophysics*, 570, 2014. ISSN 0004-6361. doi:
10.1051/0004-6361/201424358.

[59] Ramesh Narayan, Rohan Mahadevan, Jonathan E Grindlay, Robert
Popham, and Charles Gammie. ADVECTION-DOMINATED AC-
CRETION MODEL OF SAGITTARIUS A* : EVIDENCE FOR A
BLACK HOLE AT THE GALACTIC CENTER. *THE ASTROPHYS-
ICAL JOURNAL*, 492:554–568, 1998. URL `http://iopscience.`
`iop.org/article/10.1086/305070/pdf`.

[60] NASA. Mars planet facts news & images — NASA Mars rover + mission info, 2017. URL https://mars.nasa.gov/.

[61] Claudia Negulescu and Stefan Possanner. CLOSURE OF THE STRONGLY MAGNETIZED ELECTRON FLUID EQUATIONS IN THE ADIABATIC REGIME. *MULTISCALE MODEL. SIMUL. c 2016 EUROfusion Consortium*, 14(2):839–873, 2016. doi: 10.1137/15M1027309. URL http://epubs.siam.org/doi/pdf/10.1137/15M1027309.

[62] Dwight R. Nicholson. *Introduction to plasma theory*. Wiley, 1983. ISBN 047109045X.

[63] Andrzej Niedzwiecki, Fu-Guo Xie, and Agnieszka Stpnik. X-ray spectra of hot accretion flows. *MNRAS*, 443:1733–1747, 2014. doi: 10.1093/mnras/stu1262.

[64] Chris Nixon and Greg Salvesen. A physical model for state transitions in black hole X-ray binaries. *Monthly Notices of the Royal Astronomical Society*, 437(4):3994–3999, 2014. ISSN 00358711. doi: 10.1093/mnras/stt2215.

[65] Feryal Oezel and Tiziana Di Matteo. X-Ray Images of Hot Accretion Flows. *The Astrophysical Journal*, 548:213–218, 2001.

[66] B Paczynski. A Model of Self-gravitating Accretion Disk. *Acta Astronomica*, 28(2):91–109, 1978. URL http://articles.adsabs.harvard.edu/cgi-bin/nph-iarticle{_}query?1978AcA....28...91P{&}defaultprint=YES{&}filetype=.pdf.

[67] I. Parrish and E. Quataert. NONLINEAR SIMULATIONS OF THE HEAT-FLUX-DRIVEN BUOYANCY INSTABILITY AND ITS IMPLICATIONS FOR GALAXY CLUSTERS. *The Astrophysical Journal*, 677:9–12, 2008.

[68] Ian J. Parrish and James M. Stone. Nonlinear Evolution of the Magnetothermal Instability in Two Dimensions. *The Astrophysical Journal*, 633:334–348, 2005. ISSN 0004-637X. doi: 10.1086/518881. URL http://arxiv.org/abs/astro-ph/0612195.

[69] Ian J. Parrish and James M. Stone. Simulation of the magnetothermal instability. *Astrophysics and Space Science*, 307(1-3):77–82, 2007. ISSN 0004640X. doi: 10.1007/s10509-006-9243-4.

[70] I.~J. Parrish, J.~M. Stone, and N Lemaster. The Magnetothermal Instability in the Intracluster Medium. \\Apj, 688(1999):905–917, 2008. ISSN 0004-637X. doi: 10.1086/592380.

[71] Thierry Passot, D Borgogno, P Henri, P Hunana, D Laveder, L Marradi, and P L Sulem. Fluid closures: the introduction of kinetic effects, 2013. URL `http://userpages.irap.omp.eu/{~}frincon/houches/Passot.pdf`.

[72] R. F. Penna, A. Sadowski, A. K. Kulkarni, and R. Narayan. The Shakura-Sunyaev viscosity prescription with variable. *Monthly Notices of the Royal Astronomical Society*, 428(3):2255–2274, jan 2013. ISSN 0035-8711. doi: 10.1093/mnras/sts185. URL `https://academic.oup.com/mnras/article-lookup/doi/10.1093/mnras/sts185`.

[73] W. G. Pilipp, K.-H. Muehlhaeuser, H. Miggenrieder, M. D. Montgomery, and H. Rosenbauer. Characteristics of electron velocity distribution functions in the solar wind derived from the Helios plasma experiment. *Journal of Geophysical Research*, 92(5):1075–1092, 1987. ISSN 0148-0227. doi: 10.1029/JA092iA02p01075.

[74] D S Plant, R P Fender, G Ponti, T Muñoz-Darias, and M Coriat. Revealing accretion on to black holes: X-ray reflection throughout three outbursts of GX 339-4. *MN-RAS*, 442:1767–1785, 2014. doi: 10.1093/mnras/stu867. URL `https://oup.silverchair-cdn.com/oup/backfile/Content{_}public/Journal/mnras/442/2/10.1093/mnras/stu867/2/stu867.pdf?Expires=1492353626{&}Signature=LH3xW3BZE{~}VEUeXCqWtkFENGrKurqR{~}U8fPv3xoXDzZ3PG5H1ODqTe9rhsCYMQ0F8jihdYJ7I4YZ`

[75] Dimitrios Psaltis, Feryal Özel, Chi-Kwan Chan, and Daniel P Marrone. A GENERAL RELATIVISTIC NULL HYPOTHESIS TEST WITH EVENT HORIZON TELESCOPE OBSERVATIONS OF THE BLACK HOLE SHADOW IN Sgr A*. *The Astrophysical Journal*, 814:115, 2015. doi: 10.1088/0004-637X/814/2/115. URL `http://iopscience.iop.org/article/10.1088/0004-637X/814/2/115/pdf`.

[76] M I Pudovkin and Andv S Semenov. MAGNETIC FIELD RECONNECTION THEORY AND THE SOLAR WIND - MAGNETOSPHERE INTERACTION: A REVIEW. *Sci. Rev.*, 41(1):1–89, 1985. URL `http://download.springer.`

com/static/pdf/528/art{%}253A10.1007{%}252FBF00241346.
pdf?originUrl=http{%}253A{%}252F{%}252Flink.
springer.com{%}252Farticle{%}252F10.
1007{%}252FBF00241346{&}token2=exp=1492120748{~}acl=
{%}252Fstatic{%}252Fpdf{%}252F528{%}252Fart{%}2525253A10.
1007{%}2525252FBF00241346.pdf{%}253ForiginUrl{%}253.

[77] E. Quataert. Buoyancy Instabilities in Weakly Magnetized Low Collisionality Plasmas. *The Astrophysical Journal*, 673(2):758–762, 2008. ISSN 0004-637X. doi: 10.1086/525248. URL http://arxiv.org/abs/0710.5521.

[78] Ronald A Remillard and Jeffrey E Mcclintock. X-ray Properties of Black-Hole Binaries. *Annual Review of Astronomy and Astrophysics*, 44:49–92, 2006.

[79] Sean M. Ressler, A. Tchekhovskoy, Eliot Quataert, Mani Chandra, and Charles F. Gammie. Electron Thermodynamics in GRMHD Simulations of Low-Luminosity Black Hole Accretion. *Monthly Notices of the Royal Astronomical Society*, 1870(September):1848–1870, 2015. ISSN 0035-8711. doi: 10.1093/mnras/stv2084. URL http://adsabs.harvard.edu/abs/2015arXiv150904717R.

[80] Ramesh Rohan, Jonathan E Narayan, M Ahadevan, G Rindlay, Robert G And, Charles Popham, and G Ammie. ADVECTION-DOMINATED ACCRETION MODEL OF SAGITTARIUS A* : EVIDENCE FOR A BLACK HOLE AT THE GALACTIC CENTER. *THE ASTROPHYSICAL JOURNAL*, 492:554–568, 1998. URL http://iopscience.iop.org/article/10.1086/305070/pdf.

[81] L Romagnani, S V Bulanov, M Borghesi, P Audebert, J C Gauthier, K Löwenbrück, A J Mackinnon, P Patel, G Pretzler, T Toncian, and O Willi. Observation of Collisionless Shocks in Laser-Plasma Experiments. *Physical Review Letters*, 101, 2008. doi: 10.1103/PhysRevLett. 101.025004. URL https://journals-aps-org.ezproxy.princeton. edu/prl/pdf/10.1103/PhysRevLett.101.025004.

[82] Aleksander Sadowski, Jean-Pierre Lasota, Marek A. Abramowicz, and Ramesh Narayan. Energy flows in thick accretion discs and their consequences for black hole feedback. *Monthly Notices of the Royal Astronomical Society*, 456(4):3915–3928, 2016. ISSN 0035-8711. doi:

10.1093/mnras/stv2854. URL `http://mnras.oxfordjournals.org/lookup/doi/10.1093/mnras/stv2854`.

[83] Greg Salvesen, Philip J Armitage, Jacob B Simon, and Mitchell C Begelman. Strongly magnetized accretion discs require poloidal flux. *MNRAS*, 460:3488–3493, 2016. doi: 10.1093/mnras/stw1231. URL `https://oup.silverchair-cdn.com/oup/backfile/Content{_}public/Journal/mnras/460/4/10.1093{_}mnras{_}stw1231/2/stw1231.pdf?Expires=1492749004{&}Signature=YJnHMEOosBT4FRaZRRWsDVvsAcETwO{~}Kb9KbybWh{~}ZXtTTEOEObIZKFNmro6VrZ88H4rLGCbpHz2`

[84] T Sano, S-I. Inutsuka, N J Turner, and J M Stone. Angular momentum transport by MHD turbulence in accretiondisks: Gas pressure dependence of the saturation level of the magnetorotational instability. *Astrophys. J.*, 605:321–339, 2004.

[85] A A Schekochihin, S C Cowley, R M Kulsrud, M S Rosin, and T Heinemann. Nonlinear Growth of Firehose and Mirror Fluctuations in Astrophysical Plasmas. *Physical Review Letters*, 100, 2008. doi: 10.1103/PhysRevLett.100.081301. URL `https://journals.aps.org/prl/pdf/10.1103/PhysRevLett.100.081301`.

[86] Steven J Schwartz. Plasma Instabilities in the Solar Wind : Review A Theoretical. *Reviews of Geophysics*, (9):313, 1980.

[87] N. Shakura and R. Sunyaev. Black Holes in Binary Systems. Observational Appearance. *Astronomy and Astrophysics*, 24:337–355, 1973. URL `http://articles.adsabs.harvard.edu/cgi-bin/nph-iarticle{_}query?1973A{%}26A....24..337S{&}defaultprint=YES{&}filetype=.pdf`.

[88] S. Shapiro. Accretion onto Black Holes: The Emergent Radiation Spectrum. *The Astrophysical Journal*, 180:531–546, 1973. URL `http://articles.adsabs.harvard.edu/cgi-bin/nph-iarticle{_}query?1973ApJ...180..531S{&}defaultprint=YES{&}filetype=.pdf`.

[89] P. Sharma, G. Hammett, and E. Quataert. Transition from Collisionless to collisional magnetorotational instability. *The Astrophysical Journal*, 596:1121–1130, 2003. URL `http://iopscience.iop.org/article/10.1086/378234/pdf`.

[90] P. Sharma, G. Hammett, and E. Quataert. Collisional Effects on the Kinetic MRI. *ASP Conference Series*, 311:139–140, 2004.

[91] P. Sharma, E. Quataert, and J. M. Stone. Spherical accretion with anisotropic thermal conduction. *Monthly Notices of the Royal Astronomical Society*, 389(4):1815–1827, 2008. ISSN 00358711. doi: 10.1111/j.1365-2966.2008.13686.x.

[92] Prateek Sharma. Kinetic Effects on Turbulence Driven by the Magnetorotational Instability in Black Hole Accretion. *PhD Thesis, 2007*, (September), 2007. URL `http://arxiv.org/abs/astro-ph/0703542`.

[93] Prateek Sharma, Gregory W Hammett, Eliot Quataert, and James M Stone. SHEARING BOX SIMULATIONS OF THE MRI IN A COLLISIONLESS PLASMA. *The Astrophysical Journal*, 637:952–967, 2006. URL `http://iopscience.iop.org/article/10.1086/498405/pdf`.

[94] Prateek Sharma, Eliot Quataert, Gregory W Hammett, and James M Stone. ELECTRON HEATING IN HOT ACCRETION FLOWS. *The Astrophysical Journal*, 667:714–723, 2007. URL `http://iopscience.iop.org/article/10.1086/520800/pdf`.

[95] Ji-Ming Shi, James M Stone, and Chelsea X Huang. Saturation of the magnetorotational instability in the unstratified shearing box with zero net flux: convergence in taller boxes. *MNRAS*, 456:2273–2289, 2016. doi: 10.1093/mnras/stv2815. URL `https://oup.silverchair-cdn.com/oup/backfile/Content{_}public/Journal/mnras/456/3/10.1093/mnras/stv2815/2/stv2815.pdf?Expires=1488995752{&}Signature=G1P6fLVscE2-UIFgxquzdc-0Y-11JchH7OKFpWA7dxa1Dt7cxlQI{~}MlIoduHGi8mf50FNF-JXBq1U4`

[96] Hotaka Shiokawa. General Relativistic MHD Simulations of Black Hole Accretion Disks: Dynamics and Radiative Properties, 2013.

[97] Jacob B Simon and John F Hawley. VISCOUS AND RESISTIVE EFFECTS ON THE MAGNETOROTATIONAL INSTABILITY WITH A NET TOROIDAL FIELD. *The Astrophysical Journal*, 707:833–843, 2009. doi: 10.1088/0004-637X/707/1/833. URL `http://iopscience.iop.org/article/10.1088/0004-637X/707/1/833/pdf`.

[98] Jacob B Simon, John F Hawley, and Kris Beckwith. SIMULATIONS OF MAGNETOROTATIONAL TURBULENCE WITH

A HIGHER-ORDER GODUNOV SCHEME. *The Astrophysical Journal*, 690:974–997, 2009. doi: 10.1088/0004-637X/690/1/974. URL `http://iopscience.iop.org/article/10.1088/0004-637X/690/1/974/pdf`.

[99] H Spruit. Accretion Disks. In I. Martinez-Pais, T. Shahbaz, and J. Velazquez, editors, *Accretion Processes in Astrophysics*, chapter 1, pages 1–44. Cambridge University Press, 2014.

[100] J. Stone, M. Kunz, and A. Bhattacharjee. AST 521 Problem Set 1, 2016.

[101] J. M. Stone, T. a. Gardiner, P. Teuben, J. F. Hawley, and J. B. Simon. Athena: A New Code for Astrophysical MHD. *The Astrophysical Journal Supplement Series*, 178:137–177, 2008. ISSN 0067-0049. doi: 10.1086/588755. URL `http://arxiv.org/abs/0804.0402`.

[102] James; Stone and Michael Norman. Numerical Simulations of Magnetic Accretion Disks. *The Astrophysical Journal*, 433:746–756, 1994.

[103] James M Stone. The Athena MHD Code: Extensions, Applications, and Comparisons to ZEUS. *ASP Conference Series*, 406:277–286, 2009. URL `http://articles.adsabs.harvard.edu/cgi-bin/nph-iarticle{_}query?db{_}key=AST{&}bibcode=2009ASPC..406..277S{&}letter=0{&}classic=YES{&}defaultprint=YES{&}whole{_}paper=YES{&}page=277{&}epage=277{&}send=Send+PDF{&}filetype=.pdf`.

[104] James M Stone and Thomas A Gardiner. IMPLEMENTATION OF THE SHEARING BOX APPROXIMATION IN ATHENA. *The Astrophysical Journal Supplement Series*, 189:142–155, 2010. doi: 10.1088/0067-0049/189/1/142.

[105] James M. Stone, John F. Hawley, Charles F. Gammie, and Steven A. Balbus. Three-dimensional Magnetohydrodynamical Simulations of Vertically Stratified Accretion Disks. *The Astrophysical Journal*, 463 (2):656, 1996. ISSN 0004-637X. doi: 10.1086/177280. URL `http://adsabs.harvard.edu/cgi-bin/nph-data{_}query?bibcode=1996ApJ...463..656S{&}link{_}type=ABSTRACT{%}5Cnpapers2://publication/doi/10.1086/177280{%}5Cnhttp://adsabs.harvard.edu/doi/10.1086/177280`.

[106] Marek Strumik, Alexander Schekochihin, and Per Helander. Physical mechanisms of regulation of pressure anisotropy in collisionless turbulent plasmas within MHD-CGL regime. In *Fifth International Workshop on the Theory and Applications of the Vlasov equation*, Copanello, Italy, 2016. URL http://www.fis.unical.it/astroplasmi/vlasovia2016/PRESENTATIONS/VLASOVIA2016/2{_}TUESDAY/STRUMIK.pdf.

[107] J M Tenbarge, R D Hazeltine, and S M Mahajan. Fluid model for relativistic, magnetized plasmas. *Citation: Physics of Plasmas*, 15, 2008. doi: 10.1063/1.2937123. URL http://dx.doi.org/10.1063/1.2937123http://aip.scitation.org/toc/php/15/6.

[108] N J Turner, J M Stone, and T Sano. Local Axisymmetric Simulations of Magnetorotational Instability in Radiationdominated Accretion Disks. *The Astrophysical Journal*, 566(1):148–163, 2002. ISSN 0004-637X. doi: 10.1086/338081. URL http://adsabs.harvard.edu/cgi-bin/nph-data{_}query?bibcode=2002ApJ...566..148T{&}link{_}type=ABSTRACT{%}5Cnpapers2://publication/doi/10.1086/338081{%}5Cnhttp://stacks.iop.org/0004-637X/566/i=1/a=148.

[109] Alexandra Veledina, Juri Poutanen, and Indrek Vurm. Hot accretion flow in black hole binaries: A link connecting X-rays to the infrared. *Monthly Notices of the Royal Astronomical Society*, 430(4):3196–3212, 2013. ISSN 00358711. doi: 10.1093/mnras/stt124.

[110] C. White and J. Stone. *Development and application of numerical techniques for general-relativistic magnetohydrodynamics simulations of black hole accretion. - Princeton University Library Catalog.* PhD thesis, Princeton University, 2016. URL https://pulsearch.princeton.edu/catalog/10096882.

[111] Christopher J White, James M Stone, and Charles F Gammie. AN EXTENSION OF THE ATHENA++ CODE FRAMEWORK FOR GRMHD BASED ON ADVANCED RIEMANN SOLVERS AND STAGGERED-MESH CONSTRAINED TRANSPORT. *The Astrophysical Journal Supplement Series*, 225, 2016. doi: 10.3847/0067-0049/225/2/22. URL http://iopscience.iop.org.ezproxy.princeton.edu/article/10.3847/0067-0049/225/2/22/pdf.

71

[112] Feng Yuan and Ramesh Narayan. Hot One-Temperature Accretion Flows Around Black Holes. *Annual Review of Astronomy and Astrophysics*, 52:529–588, 2014. ISSN 0004-637X. doi: 10.1146/annurev-astro-082812-141003. URL `http://arxiv.org/abs/astro-ph/9601074`.

[113] Feng Yuan, Eliot Quataert, and Ramesh Narayan. NONTHERMAL ELECTRONS IN RADIATIVELY INEFFICIENT ACCRETION FLOW MODELS OF SAGITTARIUS A*. *The Astrophysical Journal*, 598:301–312, 2003.